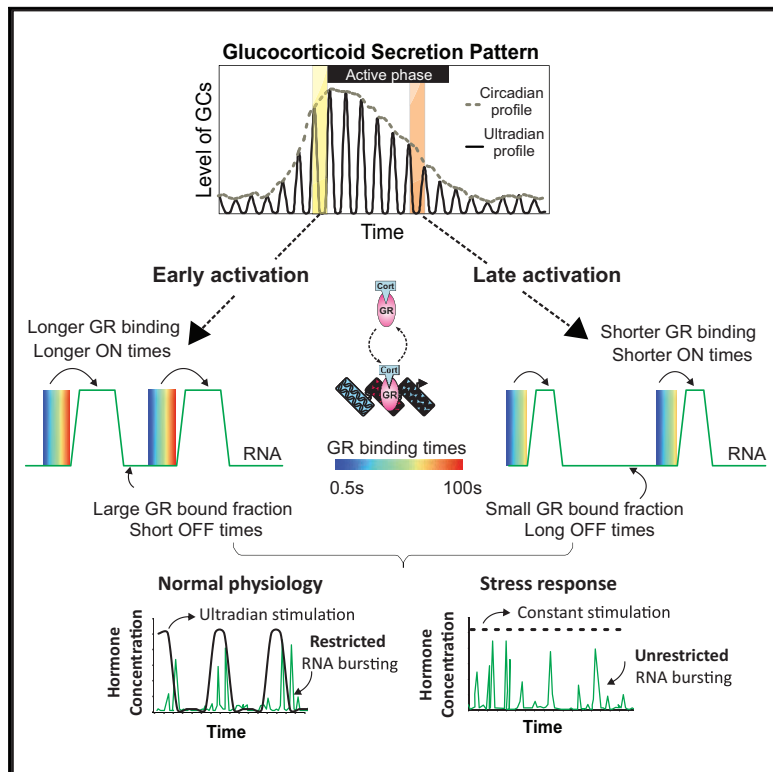


# Molecular Cell

## Transcriptional Bursting and Co-bursting Regulation by Steroid Hormone Release Pattern and Transcription Factor Mobility

### Graphical Abstract



### Authors

Diana A. Stavreva, David A. Garcia,  
Gregory Fettweis, ...,  
Gianluca Pegoraro, Arpita Upadhyaya,  
Gordon L. Hager

### Correspondence

stavrevd@mail.nih.gov (D.A.S.),  
hagerg@exchange.nih.gov (G.L.H.)

### In Brief

Stavreva et al. reveal a delay between glucocorticoid receptor (GR) binding and RNA synthesis and link GR mobility modulations in time- and treatment-dependent manner to the size and frequency of transcriptional bursts based on single molecule experiments. By reconstructing GR signaling dynamics on timescales ranging from days to milliseconds, they relate single-cell and single-molecule phenomena to glucocorticoid physiology.

### Highlights

- Circadian depletion of GCs is required for reactivation of GR target genes
- Ultradian and constant hormone treatments result in distinct RNA bursting patterns
- The GR dwell time and bound fraction determine RNA burst duration and frequency
- Stimulation with GCs induces co-bursting of proximal and distal transcription sites



# Transcriptional Bursting and Co-bursting Regulation by Steroid Hormone Release Pattern and Transcription Factor Mobility

Diana A. Stavreva,<sup>1,\*</sup> David A. Garcia,<sup>1,2</sup> Gregory Fettweis,<sup>1</sup> Prabhakar R. Gudla,<sup>1</sup> George F. Zaki,<sup>3</sup> Vikas Soni,<sup>1,5</sup> Andrew McGowan,<sup>1</sup> Geneva Williams,<sup>1</sup> Anh Huynh,<sup>4,6</sup> Murali Palangat,<sup>1</sup> R. Louis Schiltz,<sup>1</sup> Thomas A. Johnson,<sup>1</sup> Diego M. Presman,<sup>1,7</sup> Matthew L. Ferguson,<sup>4</sup> Gianluca Pegoraro,<sup>1</sup> Arpita Upadhyaya,<sup>2</sup> and Gordon L. Hager<sup>1,8,\*</sup>

<sup>1</sup>Laboratory of Receptor Biology and Gene Expression, 41 Library Drive, Center for Cancer Research, NCI, NIH, Bethesda, MD 20892-5055, USA

<sup>2</sup>Department of Physics and Institute for Physical Science and Technology, University of Maryland, College Park, MD 20742, USA

<sup>3</sup>High Performance Computing Group, Frederick National Laboratory for Cancer Research, Frederick, MD, USA

<sup>4</sup>Department of Physics and Graduate Program in Biomolecular Science, Boise State University, Boise, ID 83725, USA

<sup>5</sup>Present address: Micropulsion and Nanotechnology Laboratory, GW University, Washington, DC, USA

<sup>6</sup>Present address: Department of Biophysics, University of Michigan, Ann Arbor, MI 48109, USA

<sup>7</sup>Present address: IFIBYNE, UBA-CONICET, Universidad de Buenos Aires, Facultad de Ciencias Exactas y Naturales, Buenos Aires, Argentina

<sup>8</sup>Lead Contact

\*Correspondence: stavrevd@mail.nih.gov (D.A.S.), hagerg@exchange.nih.gov (G.L.H.)

<https://doi.org/10.1016/j.molcel.2019.06.042>

## SUMMARY

Genes are transcribed in a discontinuous pattern referred to as RNA bursting, but the mechanisms regulating this process are unclear. Although many physiological signals, including glucocorticoid hormones, are pulsatile, the effects of transient stimulation on bursting are unknown. Here we characterize RNA synthesis from single-copy glucocorticoid receptor (GR)-regulated transcription sites (TSs) under pulsed (ultradian) and constant hormone stimulation. In contrast to constant stimulation, pulsed stimulation induces restricted bursting centered around the hormonal pulse. Moreover, we demonstrate that transcription factor (TF) nuclear mobility determines burst duration, whereas its bound fraction determines burst frequency. Using 3D tracking of TSs, we directly correlate TF binding and RNA synthesis at a specific promoter. Finally, we uncover a striking co-bursting pattern between TSs located at proximal and distal positions in the nucleus. Together, our data reveal a dynamic interplay between TF mobility and RNA bursting that is responsive to stimuli strength, type, modality, and duration.

## INTRODUCTION

Glucocorticoid receptor (GR) activation of the mouse mammary tumor virus (MMTV) promoter is one of the first model systems used to study transcription in single cells (Ko et al., 1990). These experiments revealed the stochastic nature of transcription because only a subpopulation of the cells responded to the acti-

vating signal. Subsequent studies have demonstrated that genes are transcribed in short stochastic bursts, followed by much longer periods of inactivity (Bahar Halpern et al., 2015; Chubb et al., 2006; Fritzsch et al., 2018; Golding et al., 2005; Larson et al., 2011; Lenstra et al., 2015; Paré et al., 2009; Raj et al., 2010; Rodriguez et al., 2019; Suter et al., 2011a, 2011b; Zenklusen et al., 2008). Both burst size and frequency are amenable to modulation (Bartman et al., 2016; Cai et al., 2008; Dar et al., 2012; Ferguson et al., 2012; Fukaya et al., 2016; Larson et al., 2013; Nicolas et al., 2018), and, in some cases, different stimuli can trigger kinetically distinct transcriptional responses of the same gene (Molina et al., 2013).

Transcription factors (TFs) involved in transcription regulation interact dynamically with chromatin targets (Hager et al., 2009). It has recently become possible to observe individual TF molecules in live cells using single-molecule tracking (SMT) (Ball et al., 2016; Chen et al., 2014; Gebhardt et al., 2013; Izeddin et al., 2014; Kitagawa et al., 2017; Mazza et al., 2012; Morisaki et al., 2014; Normanno et al., 2012; Paakinaho et al., 2017; Speil et al., 2011; Sugo et al., 2015; Swinstead et al., 2016). By using synthetic TFs and RNA fluorescence *in situ* hybridization (FISH), an earlier study had associated the strength of the TF transactivation domain with transcription initiation and burst duration with the TF binding time at a promoter (Senecal et al., 2014). Another study used a synthetic, optogenetically regulated TF to address transcriptional regulation in yeast (Rulan et al., 2018), and a more recent study demonstrated a connection between a yeast TF and transcriptional bursting (Donovan et al., 2019). However, it is still unclear how *bona fide* mammalian TFs regulate bursting.

Many physiological signals and regulatory proteins, including TFs, exhibit pulsatile activation (Levine et al., 2013; Stavreva et al., 2012b), and a few studies have suggested that pulsatile signaling is associated with reduced cell-to-cell gene expression variability (Benzinger and Khammash, 2018; Corrigan and



Chubb, 2014). Glucocorticoids (GCs), the GR-activating hormones, are also pulsatile. They are released from the adrenal glands in a circadian (Migeon et al., 1956) as well as ultradian manner, with a periodicity of approximately 1 h (Henley et al., 2009; Lightman et al., 2008; Seale et al., 2004). This pattern is maintained at the level of extracellular fluid (Droste et al., 2008) and leads to pulsatile release of nascent RNA (Conway-Campbell et al., 2010; George et al., 2017; McMaster et al., 2011; Ono et al., 2015; Stavreva et al., 2009, 2015). In contrast, a constant hormone level, which is associated with stress (Russell et al., 2015), leads to continuous RNA synthesis (Stavreva et al., 2009, 2015). Although physiologically relevant, little is known about the interplay between the intrinsic RNA bursting pattern and the extrinsic circadian and ultradian fluctuations of GCs. Being essential for life, both under- and overproduction of GCs are associated with serious health problems (Aulinas and Webb, 2014; Feelders et al., 2012; Nieman and Ilias, 2005). Thus, insights into GC action may provide better treatment strategies for conditions where GC signaling is dysregulated.

We used an *MMTV* promoter-based cell reporter system with several unique features that allowed us to explore the relationship between hormone release pattern, GR dynamics, and RNA bursting: (1) direct GR binding of the *MMTV* promoter, (2) simplification of the activating inputs because *MMTV* is not regulated by enhancers, and (3) no transcription-related negative or positive influences because the product of *MMTV* activation has no role in promoter regulation. Thus, the *MMTV* promoter-reporter is likely to function as a generic sensor of GR activation.

We employed a high-throughput imaging and analysis platform to characterize the real-time synthesis of fluorescently labeled RNA from GR-regulated *MMTV* transcription sites (TSs). We found that ultradian stimulation induces RNA bursting that is restricted to the time of the hormonal pulse. In contrast, constant treatment results in “unrestricted” bursting comprised of short ON periods and larger OFF periods. Moreover, we found that circadian cycle-dependent depletion of the activating hormone is required for *MMTV* promoter transcriptional reactivation. Importantly, we demonstrated that the TF dwell time, as measured by SMT, determines the size of the bursts, whereas the fraction of the transiently bound receptors determines the initiation frequency. By tracking the TSs in three dimensions, we could directly correlate TF binding and RNA synthesis at the single-promoter level. Finally, we discovered that neighboring TSs as well as pairs of TSs located near the nuclear periphery were likely to co-burst, suggesting that both the local micro-environment and the nuclear periphery modulate bursting.

The results provide a comprehensive picture of GR signaling on timescales of days, hours, seconds, and milliseconds and relate single-molecule and single-cell phenomena to GC physiology.

## RESULTS

### Time-Dependent Downregulation of *MMTV* Transcription

The GR is a TF that translocates from the cytoplasm to the nucleus (Figure 1A, inset) in response to GCs. These hormones

(cortisol in humans and corticosterone in rodents) are released from the adrenal glands in a circadian and ultradian manner (Henley et al., 2009; Lightman et al., 2008; Seale et al., 2004; Veldhuis et al., 1989; Figure 1A). Physical and psychological stress stimulate GC release and continuous GR activation (Russell et al., 2015). The effects of the pulsed and continuous hormone stimulation on GR-activated genes are distinct, leading to pulsatile or continuous synthesis of nascent RNAs, respectively (Figure 1B). However, it is unclear how they arise from the activity of individual promoters.

To study GC signaling at the single-promoter level, we generated a promoter-reporter system based on the GR-responsive *MMTV* promoter driving the expression of PP7 stem loops (Figure 1C). In this system, RNA synthesis can be observed in real time upon binding of the GFP-tagged PP7 coat protein (PCP-GFP) to the newly synthesized RNA (Chao et al., 2008; Larson et al., 2011). This reporter construct was flanked by CCCTC-binding factor (CTCF) binding sites and 4 kb of Tet operator (TetO) repeats (Roukos et al., 2014) to minimize the effect of the local integration environment (Figure 1C; Figure S1A) and stably integrated into multiple loci in the genome of mouse mammary carcinoma cells (C127) expressing PCP-GFP. A subclone (33AP1C9) with 4 integration sites was selected for further analysis. Bright green foci, representing active TSs, were observed in the nuclei (Figure 1D) upon stimulation with corticosterone (Cort) or the synthetic GC dexamethasone (Dex). These cells exhibited typical time and concentration-dependent transcription activation in response to Cort and Dex (Figures S1B and S1C). Dose-response curves were used to determine the saturating levels for both hormones (600 nM for Cort and 100 nM for Dex) and were utilized in the remaining experiments. High-throughput time-lapse microscopy revealed robust *MMTV* transcription upregulation followed by progressive downregulation. This time-dependent downregulation of the *MMTV* promoter has been reported previously (Hager et al., 2006; Voss et al., 2009) and persisted for over 60 h (Figure 1E). Single-molecule RNA (smRNA) FISH analysis (Figure 1F; Figures S1G–S1J) of cells stimulated for 0, 1, 4, 6, and 12 h demonstrated hormone-specific promoter shutdown (Figures 1G and 1H). The intensity of the TS-associated RNA also diminished over time (Figure S1K). We concluded that the time-dependent downregulation of *MMTV* transcription could be used to study both high- and low-activity states in the same system.

Because GC levels in mammals are low during the inactive phase of their circadian cycle, we reasoned that this dip in hormone concentration might be required for robust gene reactivation. Indeed, 12 h of hormone withdrawal re-sensitized the system, leading to a second peak of *MMTV* activity (Figure 1I). Considering the role of GCs in the circadian cycle (Bal-salobre et al., 2000; Nicolaides et al., 2014; Schibler et al., 2015), we tested the effects of constant and pulsatile hormone stimulation on expression of the Per1 gene. The Per/CRYPTOCHROME (CRY) complex is a component of the negative arm of the transcription-translation loop of the circadian cycle, and, as shown in Figure 1J, constant GC stimulation affected Per1 transcription cycling (Figure S1L). These results and the fact that many endogenous genes are activated only transiently (John et al., 2009), suggest that a lack of hormone

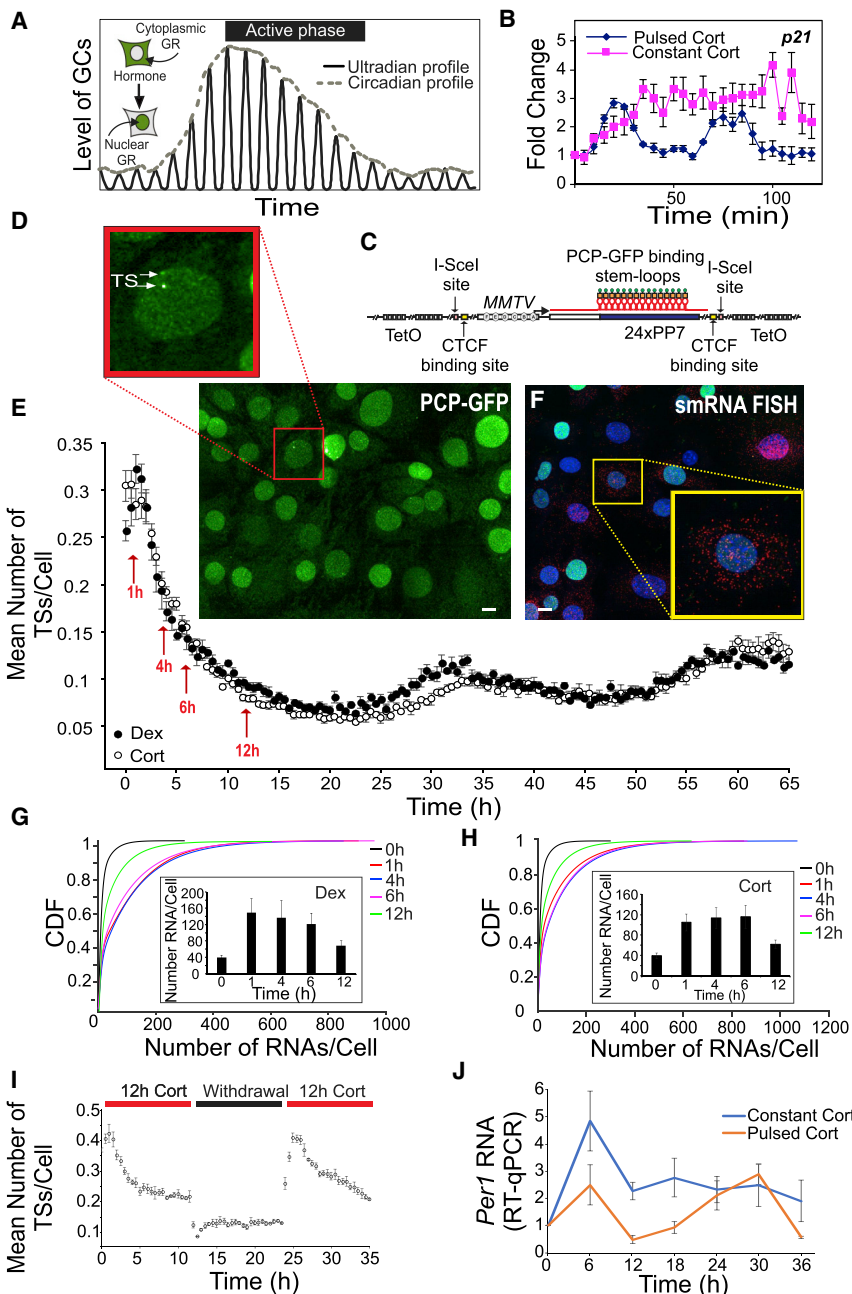


**Figure 1. MMTV Transcription Downregulation Is Relieved by Hormone Withdrawal**

(A) Schematic of the GC secretion pattern.

(B) Ultradian stimulation induces cyclic *p21* gene activation at the population level, as measured in 3134 cells by qRT- PCR, whereas constant hormone treatment induces continuous RNA synthesis. Error bars represent the mean  $\pm$  SEM;  $n = 4$ .

(C) Schematic of the *MMTV*-PP7 reporter construct.

(D) *MMTV* transcription sites (TSs) are visualized by binding of the GFP-tagged PP7 coat protein (PCP-GFP) to the newly synthesized RNA (scale bar, 5  $\mu$ m).

(E) Activation of *MMTV*-PP7 upon treatment with natural or synthetic hormone (Cort and Dex, respectively) is followed by progressive downregulation. Error bars represent the mean  $\pm$  SEM;  $n = 6$  wells.

(F) smRNA FISH with probes tagging the PP7 stem loops (red) corroborates *MMTV* induction followed by transcription downregulation. The nucleus is stained with DAPI (blue), and the green staining indicates PCP-GFP (scale bar, 5  $\mu$ m).

(G and H) The cumulative distribution frequency (CDF) curve fit corresponding to the 6-h Dex treatment (pink) significantly differs from those for 1 h and 4 h treatment (G). In contrast, RNA synthesis after 6 h Cort treatment is higher than after 1 h treatment but equivalent to the 4-h treatment (H). In both cases, 12 h after activation, the number of RNA molecules was diminished (green curves in G and H).

(I) *MMTV* transcription downregulation was alleviated by 12 h of hormone withdrawal. Error bars represent the mean  $\pm$  SEM;  $n = 6$  wells.

(J) Constant hormone treatment (600 nM Cort) interfered with the circadian cycling of the *Per1* gene ultradian treatment (Figure S1L) did not. Error bars represent the mean  $\pm$  SEM;  $n = 4$ .

withdrawal during the inactive phase perturbed the circadian cycle while also dampening the responsiveness of these GR-regulated target genes.

#### Transcription Bursting Is Modulated by the Pattern of Hormone Delivery and the Ligand Type

To achieve robust analysis, we used a high-throughput confocal imaging system and a custom analysis pipeline (Figure S2A). The presence of multiple TSs in the nuclei, the cell mobility, and the rotation of nuclei during the time-lapses, however, made tracking the intensity of individual TSs challenging. To overcome these issues, we introduced a DNA stain compatible with live-

cell imaging (silicon-rhodamine–Hoechst DNA stain [SiR-DNA]; Figures 2A–2C; Lukinavičius et al., 2015). Because the SiR-DNA fluorescence texture features remained relatively unchanged during the experiment, the SiR-DNA channel was used for both nuclear tracking and rigid body registration of the nucleus over time (Videos S1 and S2). This information was

then used to register the GFP channel, resulting in “digital immobilization” of the nucleus and reliable TS tracking (Figure S2B).

We next tested the effects of constant hormone stimulation with Dex and Cort on RNA bursting, and a typical RNA trace is shown in Figure 2D. The duration of the bursts (ON periods) was narrowly distributed, whereas the duration of the OFF periods was broadly distributed (Figure 2E; Figure S2C). Importantly, we discovered that both the ON and OFF times were ligand-dependent. Cort treatment induced longer but less frequent burst ( $8.4 \pm 0.2$  min ON time,  $36.2 \pm 1.06$  min OFF time) than Dex treatment ( $7.8 \pm 0.2$  min ON time and  $32.3 \pm 1$  min OFF time) (Figures 2F and 2G). We further validated these

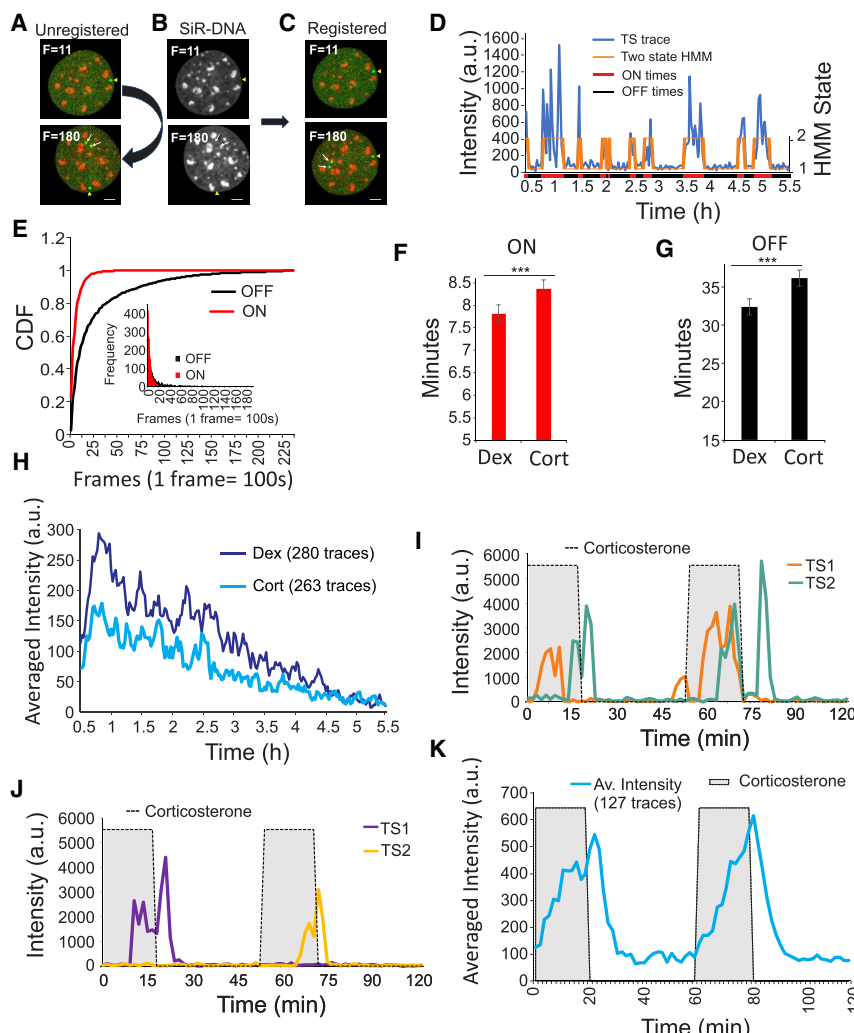


**Figure 2. Live-Cell High-Throughput Imaging Reveals Hormone- and Pattern-Specific RNA Bursting**

(A) Tracking of the transcriptional activity of multiple TSs by high-throughput imaging requires nucleus registration. A representative nucleus with a single active TS (yellow arrowhead at 3 o'clock) at frame 11 (frame = 60 s). Two additional TSs are visible in frame 180 (white arrows), and the initial TS is now at 6 o'clock (yellow arrowhead) because the cell nucleus has rotated. The PCP-GFP is shown in green, and the DNA labeled with SiR-DNA is shown in red. Scale bar, 2  $\mu$ m. Images are derived from the time lapse shown in [Video S1](#).

(B and C) Nuclear registration using the SiR-DNA staining (B) preserves the positions of the TSs over time (C). A time lapse of the registered nucleus is shown in [Video S2](#), and the corresponding RNA intensity traces are shown in [Figure S2B](#).

(D) RNA bursting profile from a representative TS comprised of intermittent ON (red) and OFF (black) periods, delineated by the two-state hidden Markov model (HMM) fit to the raw data (orange).

(E) CDF and the corresponding histogram (inset) for cells treated with Cort for 6 h, demonstrating the difference between the ON (red) and the OFF (black) time. Kolmogorov-Smirnov (KS) test,  $p = 4.44e-15$ . (F and G) Comparison of transcription bursting in response to Cort (F) and Dex (G). Student's t test was performed to calculate p values ( $***p < 0.05$ ).

(H) The average of the normalized RNA intensities recapitulated the MMTV transcription activity at the population level and time-dependent transcription downregulation.

(I and J) Two Cort pulses induced restricted RNA bursting, and TSs responded to both (I) or to just one of the pulses (J).

(K) Averaging the normalized intensities of traces recapitulates the cyclic RNA synthesis detected at the population level upon pulsatile Cort stimulation ([Figure 1B](#)). Number of analyzed traces: constant Dex 6 h,  $n = 280$ ; constant Cort 6 h,  $n = 263$ ; constant Cort 6–12 h,  $n = 115$ ; constant Dex 6–12 h,  $n = 89$ ; pulsed Cort,  $n = 127$ .

findings by imaging cells for up to 12 h and manually analyzing the RNA traces using the TrackRecord software (Mazza et al., 2013). These analyses confirmed the hormone-specific differences in ON and OFF times (Figures S2D–S2I). By averaging the normalized intensities of individual traces, we recapitulated the previously observed transcription shutdown (Figures 2H and 1E). We then studied the effects of pulsatile hormone stimulation on RNA synthesis at individual TSs by subjecting the cells to two Cort pulses. As shown in Figures 2I and 2J, these pulses induced transcriptional bursting activity restricted to the period of the hormone pulse and several minutes afterward. Some TSs responded to both pulses with one or two RNA bursts (Figure 2I), whereas others skipped either the first or the second pulse (Figure 2J). The averaged normalized intensity of over 120 traces (Figure 2K) recapitulated the RNA pulsing. Thus, restricted RNA bursting is responsible for the previously observed pulsing of nascent RNA at a population level (Stavreva et al., 2009, 2015).

### Time-Dependent Downregulation of MMTV Transcription Is Accompanied by Reduced Burst Duration and Frequency

To understand the time-dependent transcription shutdown at the single-promoter level, we compared RNA bursting in the first 6 h upon Cort activation with bursting during later activation (6–12 h). As shown in Figure 3A, the burst length (ON time) was reduced over the time of the treatment (from  $8.4 \pm 0.2$  min to  $7.0 \pm 0.3$  min), whereas the OFF time was increased ( $36.2 \pm 1.06$  min compared with  $51.8 \pm 2.6$  min; Figure 3B). These effects were preserved irrespective of the ligand (Figures 3C and 3D). Representative traces from the early and the late activation times are shown in Figures S3A and S3B. We also performed several confirmatory experiments on a Zeiss LSM780 microscope using low laser power (0.2%) and a photon-counting mode with less than 5% of bleaching throughout the time lapse. As shown in Figure S3C, RNA bursts were longer and more frequent during the first 6 h of activation. Western blot analysis did not detect

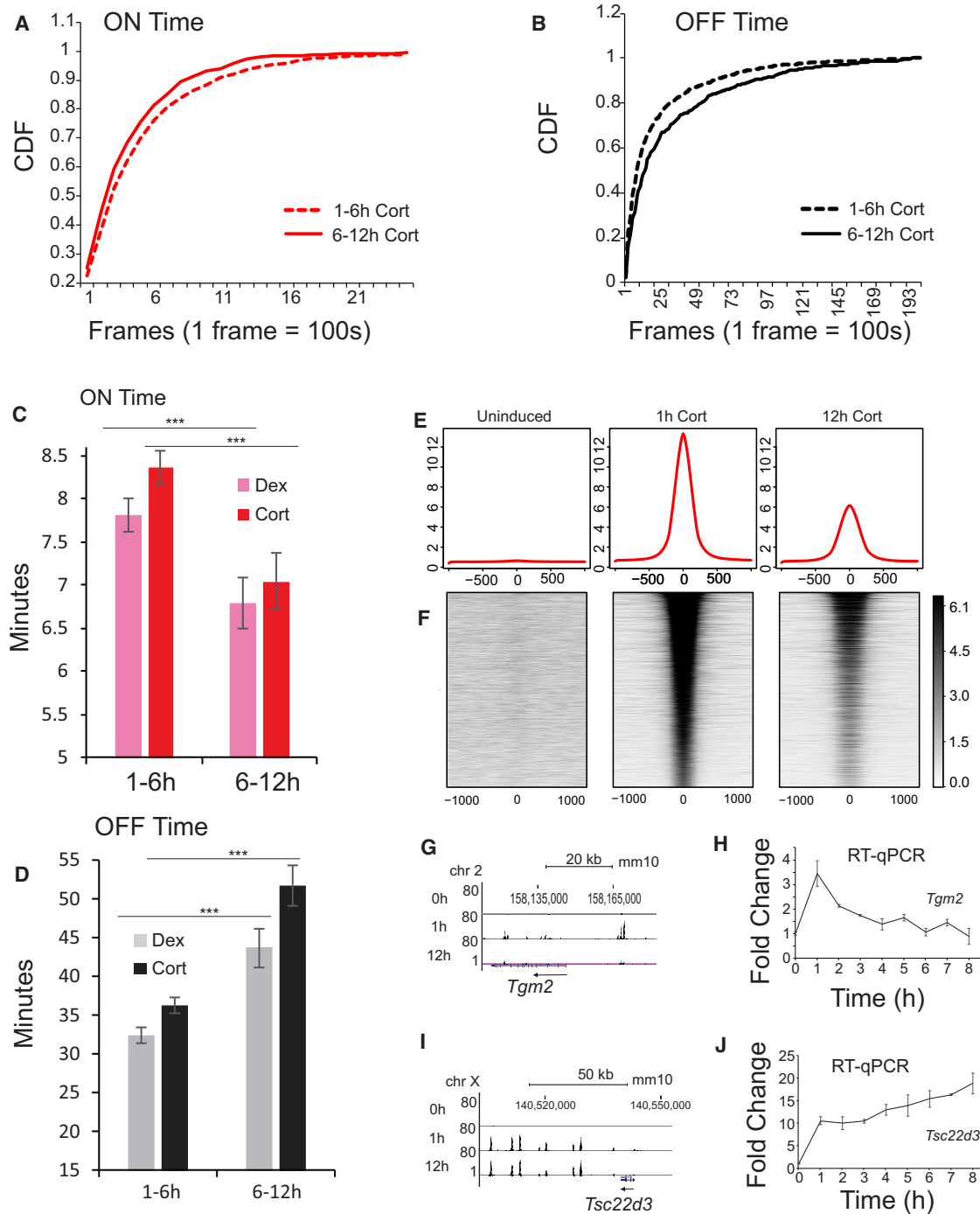


**Figure 3. Reduction in Burst Duration and Frequency over the Treatment Time**

(A) The length of the bursts (ON time) shortens over the time of treatment. The activity of the TSs was recorded at 100-s intervals during 6 h of stimulation with Cort (1–6 h) and compared with the activity recorded for the 6–12 h after stimulation. The left shift of the CDF for the late activation time (solid red curve) indicates a reduction of burst length (KS test,  $p = 0.003$ ).

(B) In contrast, the OFF periods became longer over the time of treatment (KS test,  $p = 0.0007$ ).

(C and D) These differences were observed with both the natural (C) and the synthetic (D) hormone (Cort and Dex, respectively). Student's t test was performed to calculate p values (\*\* $p < 0.05$ ).

(E) Histograms representing the average tag count of all GR ChIP-seq peaks over a 2-kb region for untreated 33AP1C9 cells and for cells treated with Cort for 1 h and 12 h.

(legend continued on next page)

significant changes in GR protein levels at 1 h versus 12 h of hormone stimulation (Figure S3D); however, visualization of GR by immunostaining with an anti-GR antibody and quantification of the signal demonstrated a significant reduction (~40%) that was not due to GR re-localization to the cytoplasm but, rather, due to its progressive degradation following hormone treatment (Figures S3E and S3F). Moreover, GR binding to the *MMTV* promoter was significantly reduced 12 h after hormone addition (Figure S3G). Importantly, GR chromatin immunoprecipitation sequencing (ChIP-seq) analysis (Figures 3E and 3F) revealed reduced GR binding to GR response elements (GREs) on the genomic scale. These changes were specifically observed at GREs involved in the regulation of genes, which, similarly to *MMTV*, underwent time-dependent transcription downregulation (Figures 3G and 3H, Figure S3H). However, there was no effect on GR binding at GREs involved in the regulation of GR-responsive genes, which did not exhibit time-dependent downregulation (Figures 3I and 3J; Figure S3I). These results suggested that the effects were locus-specific. We concluded that transcription downregulation of the *MMTV* promoter over time is achieved by reductions in GR levels and subsequent reductions in burst duration and frequency.

### GR Dwell Time Determines Burst Duration, and Its Bound Fraction Determines Burst Frequency

To address the relationship between RNA bursting and GR dynamics, we developed a new cell line (D4B2D10), expressing haloalkane dehalogenase (HALO)-tagged GR (Morisaki et al., 2014) in the background of a complete knockout of the endogenous GR (Paakinaho et al., 2017). These cells harbored six integrations of the *MMTV*-PP7 and stably expressed GFP-PCP to allow visualization of *MMTV* transcription (Figure 4A, inset). Using the high-throughput approach (Figure S2A) to study *MMTV* transcriptional bursting in this cell line (Figures S4A and S4B), we found that the average length of the ON period for D4B2D10 cells was shorter than the mean ON period measured for 33AP1C9 cells in the first 6 h after Cort activation ( $6.6 \pm 0.5$  min versus  $8.4 \pm 0.2$  min, respectively). The differences between the OFF periods upon Cort treatment were even larger ( $36.2 \pm 1.06$  min for 33AP1C9 cells versus  $49.7 \pm 2.6$  min for D4B2D10 cells). Nevertheless, these cells exhibited the typical *MMTV* activation by GCs, followed by transcription downregulation (Figure 4A). Consistent with the data from the 33AP1C9 cells, we found that the mean OFF time with Dex was larger than the mean OFF time with Cort ( $49.7 \pm 2.6$  min versus  $42.5 \pm 2$  min; Figure S4C), but, surprisingly, the mean ON times were not significantly different between these treatments ( $6.3 \pm 0.3$  min versus  $6.6 \pm 0.5$  min; Figure S4D). These results suggested that either the hormone-dependent differences found in the 33AP1C9 cell line (expressing endogenous GR) did not

hold true for D4B2D10 cells or that the 100-s interval imaging frequency was too coarse to resolve any potential differences. To test for the latter possibility, we treated D4B2D10 cells with Dex or Cort for 30 min (to allow complete translocation of the GR) and then imaged them for an additional 30 min at 10-s intervals. As shown in Figure S4E, the 10-s traces gave a more detailed view of the burst lengths and shapes than the 100-s traces. The combination of the high sampling rate and the fact that bursting is more frequent at early activation times resulted in traces with very short OFF periods. Moreover, because of the high-resolution sampling, the RNA intensity traces were lacking well-defined transitions between the ON and OFF periods (Figure S4E) and were unsuitable for the hidden Markov fit. Therefore, autocorrelation of the RNA fluorescence intensity traces as described in Cai et al. (2008) was used to extract burst duration (Figure S4F). The data were best fitted by a double exponential fit (red curve in Figure S4F), suggesting a contribution of two distinct populations. By examining the intensity traces, we noticed that some of the bursts were sharp and “simple,” whereas others were broad and “complex” (Figure S4F, inset). It should be noted that the mean burst length determined with the high sampling resolution (10 s) was less than 2 min for simple bursts after Cort treatment ( $115.6 \pm 2.4$  s), whereas the value obtained using the hidden Markov model (HMM) fit ( $6.6 \pm 0.5$  min) was closer to the duration of the complex bursts ( $580 \pm 22.3$  s or ~9.7 min). We concluded that the HMM fit was a robust but less precise way to determine the ON time but was well-suited for detection of the OFF time. Nevertheless, a comparison of the burst duration for the early and late activation times upon Cort treatment (0.5–1 h versus 11.5–12 h; red arrows in Figure 4A) demonstrated that the length of both types of bursts decreased over time (Figures 4B and 4C). We concluded that the GR response in D4B2D10 cells shared all essential features found in 33AP1C9 cells and was a reliable system in which we could examine the interplay between GR binding and RNA bursting.

Indeed, if GR binding regulates RNA bursting, then we anticipate that the GR dwell time would change with increased treatment duration. To test this, we utilized a custom-made HILO (highly inclined and laminated optical) microscopy system to track individual GR molecules labeled with an organic dye, JF549 (Grimm et al., 2015), which covalently binds the HALO tag of the GR (Figure 4D). Representative kymographs derived from cells treated with Cort for 1 h or 12 h, respectively, are shown in Figure 4E (see also Figures S4G and S4H as well as Videos S3 and S4). Analysis revealed that the resulting population of binding times had a very broad distribution, reflecting nuclear heterogeneity and the presence of thousands of GREs, likely with varying affinities for the GR. This heterogeneous population was best described by a power law fit, in which the power

(F) Heatmaps representing the binding intensity of the GR for the same three conditions. These heatmaps are presented as number of reads per  $10^6$  sequences in a 2-kb region flanking the peak center.

(G) Representative genomic region (University of California, Santa Cruz [UCSC] browser shot) illustrating the reduction in GR binding over time at GREs upstream of the transcription start site (TSS) of the *Tgm2* gene.

(H) This gene, similarly to the *MMTV* promoter, underwent time-dependent transcription downregulation. Error bars represent the mean  $\pm$  SEM; n = 3.

(I and J) GR binding to GREs associated with regulation of the *Tsc22d3* gene (Stavreva et al., 2015) was not affected (I). Consequently, this gene did not undergo time-dependent transcription shutdown (J). qRT-PCR data were from experiments using the 3134 cell line. Error bars represent the mean  $\pm$  SEM; n = 3.

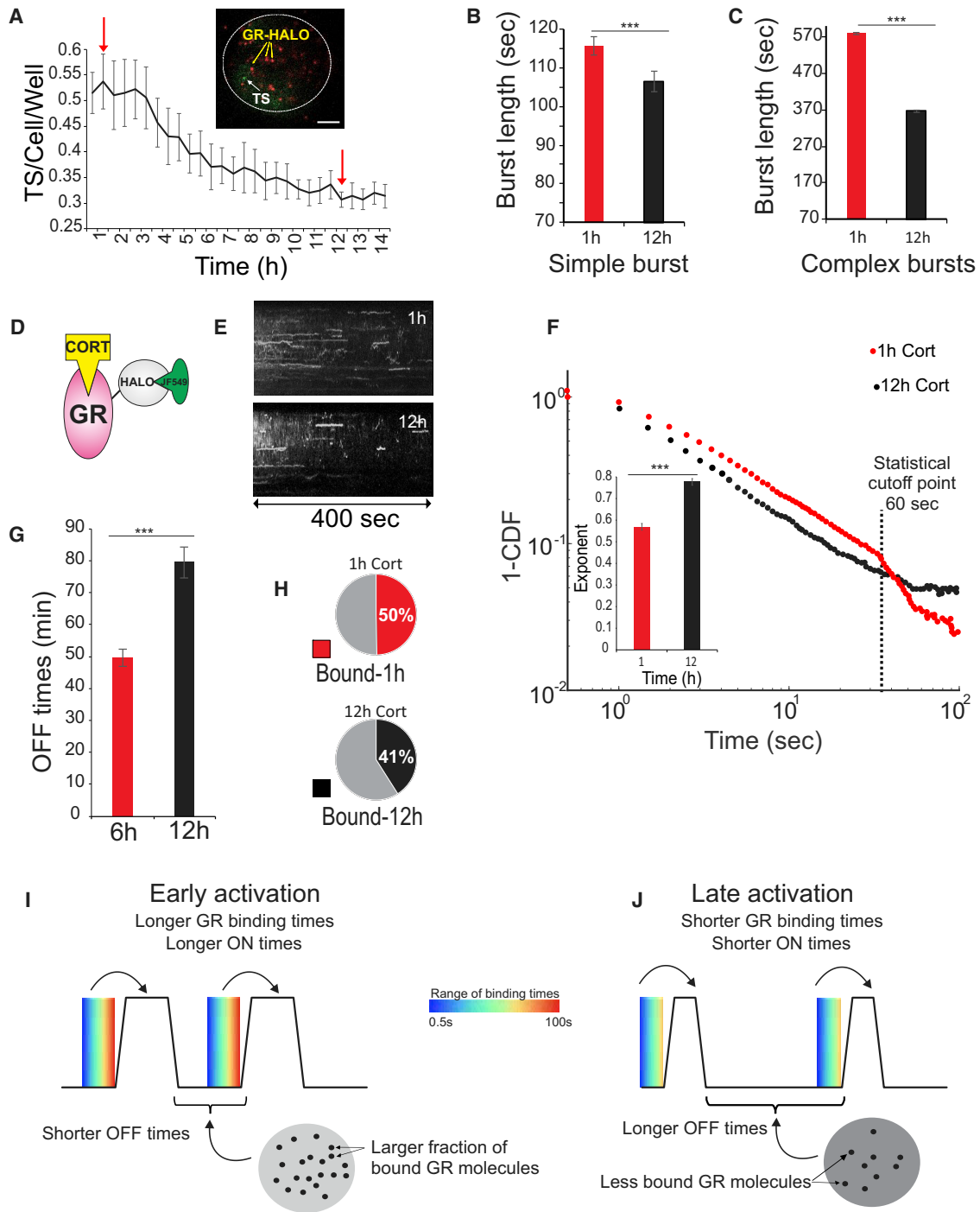


**Figure 4. GR Dwell Time Determines Burst Length, and Its Bound Fraction Determines Burst Frequency**

(A) D4B2D10 cells containing 6 copies of the stably integrated MMTV-PP7 reporter gene and expressing only HALO-tagged GRs (inset; scale bar, 2  $\mu$ m) were used to compare transcription bursting at early and late activation times (red arrows) with GR dynamics by SMT.

(B and C) A time-dependent decrease in the burst length for both simple (B) and complex (C) bursts. Student's t test was performed to calculate p values (\*\*p < 0.05).

(D) Schematic of a HALO-tagged GR with covalently bound organic JF549 dye.

(E) Representative kymographs of GR binding 1 h and 12 h after hormone treatment. The kymographs represent 800 frames of fluorescence images collected on a HILO microscope at a rate of 2 Hz with 500-ms exposure time. Additional kymographs derived from Videos S3 and S4 are shown in Figures S4G and S4H.

(F) GR behavior at the single-molecule level was best described by a power law, reflecting the broad range of binding times at the GREs throughout the nucleus. The data, when plotted on a log $\log$  scale were best fitted by a straight line and well-described by the value of the exponent. The 1-h treatment data points

(legend continued on next page)

law exponent determines the scaling of the distribution. A smaller power law exponent of the residence time distribution would imply a higher probability to find longer events and can therefore be interpreted as an overall increase in residence time. Consequently, the power law exponent can also be interpreted as the slope of the residence time distribution in a log scale (for specific details see [Garcia et al., 2019](#)). Comparison of 1 h and 12 h after activation revealed a decline in binding times ([Figure 4F](#)), reflected in an increase in the power law exponent from  $0.57 \pm 0.02$  to  $0.78 \pm 0.01$  ([Figure 4H](#), inset), which correlated with shorter burst lengths ([Figures 4B and 4C](#)). The increase in the mean OFF period from  $49.7 \pm 2.7$  min to  $79.5 \pm 5$  min over the time of Cort stimulation ([Figure 4G](#)) was inversely related to the fraction of the GR-bound molecules,  $49.7\% \pm 0.95\%$  versus  $41\% \pm 0.89\%$ , for 1 h and 12 h of Cort treatment, respectively ([Figure 4H](#)). We concluded that TF binding determines the length of the RNA bursts, which was consistent with earlier reports ([Senecal et al., 2014; Donovan et al., 2019](#)). We also found that the proportion of bound molecules determined the burst frequency ([Figures 4I and 4J](#)).

#### Ligand-Specific Changes in RNA Bursting Are Associated with Changes in GR Dynamics

We have determined that treatment with Dex induced shorter but more frequent bursts than treatment with Cort ([Figures 2F and 2G](#)) in both 33AP1C9 and D4B2D10 cells ([Figures 5A and 5C](#)). If our conclusion that GR dwell time at the promoter indeed determined burst length, we would expect that the GR residence time with Cort would be longer than the GR dwell time with Dex. This was confirmed by exposing D4B2D10 cells to Cort or Dex for 1 h and performing SMT ([Figure 5B](#)). The data were again best described by a power law ([Figures S5A and S5B](#)), and the resulting exponent values were  $0.57 \pm 0.02$  and  $0.72 \pm 0.02$  for Cort and Dex, respectively. Moreover, we found a smaller bound fraction with Cort than with Dex ( $47.9\% \pm 2\%$  versus  $64.6\% \pm 1.8\%$ , respectively; [Figure 5D](#)), which correlated well with the longer OFF periods associated with Cort treatment ([Figure 5C](#)). To further validate these findings, we stably integrated the HALO-tagged GR into the genome of 33AP1C9 cells and performed SMT. As shown in [Figure 5E](#), the exponent values for the GR with Cort and Dex after 1 h stimulation were  $0.64 \pm 0.02$  and  $0.76 \pm 0.01$ , respectively. This is consistent with the observed longer bursts upon Cort treatment ([Figure 2F](#)). In agreement with the longer OFF periods upon Cort rather than Dex treatment ([Figure 2G](#)), the GR-bound fraction was smaller after treatment with Cort than with Dex ([Figure 5F](#)). These experiments confirmed that GR dwell times are correlated with burst size, whereas the percentage of the transiently bound receptors

determined the OFF time or initiation frequency ([Figures 5G and 5H](#)).

#### Simultaneous Measurement of the GR and RNA Intensity at the MMTV Locus

To further study the relationship of GR binding and RNA synthesis, we employed the 3D orbital tracking (3DOT) method ([Annibale and Gratton, 2015; Donovan et al., 2019; Kis-Petikova and Gratton, 2004; Levi et al., 2003, 2005a, 2005b](#)), which allows simultaneous measurement of the intensity of the HALO-tagged GR molecules and the GFP-tagged RNA at an individual TS. For the majority of the 3DOT experiments ([Figure 6A](#)), we used the D4B2D10 cell line, in which the GR molecules are HALO-tagged. Because the 3DOT microscopy system was optimized for 488- and 633-nm lasers, we used JF646 dye ([Grimm et al., 2016](#)) to visualize the GR molecules instead of JF549, which was used in the previously discussed SMT experiments. Considering that the burst frequency was highly reduced at late activation times ([Figure 4G](#)), we restricted our measurements to the first 2–3 h after induction. We also chose Dex induction over Cort because the frequency of bursting is higher with Dex ([Figure 5C](#)), making observation of closely spaced bursts more likely. Representative traces of the experiments are shown in [Figure 6B](#) and [Figure S6A](#). The intensity profiles of the GR (red) and RNA (green) over time revealed peaks of GR binding, representing binding of multiple GR molecules at the MMTV locus, followed by increased RNA transcription ([Figure 6B; Figure S6A](#)). Autocorrelation and cross-correlation analysis ([Figure 6C](#)) and the assumption that GR binding induces RNA synthesis were used for interpretation of the results ([Figure S6B](#)). The autocorrelation analyses revealed an average GR binding time of  $56 \pm 5.2$  s, which is within the range of the power law distribution for GR dwell times (0.5–100 s) measured by SMT ([Figure 6C](#)). The average RNA dwell time was  $156 \pm 5.5$  s. Similar values were obtained for the 33AP1C9 cell line, in which HALO-tagged GR was expressed in addition to the endogenous GR ([Figure S6C](#)). Consistent with the assumption that GR binding leads to RNA synthesis ([Figure S6B](#)), we obtained a positive red (GR) to green (RNA) cross-correlation (blue curve in [Figure 6C](#)). The right shift of the center of the cross-correlation curve reflected a delay of  $182 \pm 1.4$  s between these two events. A similar, albeit shorter delay ( $\sim 80$  s) was recently reported between Gal4 binding and GAL10 transcription in yeast ([Donovan et al., 2019](#)). The temporal correlation was undetectable in the negative controls ([Figures S6D and S6E](#)).

We concluded that binding of multiple GR molecules was responsible for the activation of transcription at the MMTV locus ([Figure 6D](#)) and that these events were separated in time.

(red dots) were above those of the 12-h treatment (black dots). Consequently, the power law exponent of the 1-h dataset was smaller than the exponent of the 12-h dataset, as illustrated in the inset. Student's t test was performed to calculate p values (\*\*p < 0.05).

(G) The OFF time measured for the first 6 h after Cort treatment was shorter than the OFF time for the later 6–12 h ( $49.7 \pm 2.7$  min versus  $79.5 \pm 4.9$  min, respectively). Data were derived from the RNA intensity traces collected at 100-s intervals. Student's t test was performed to calculate p values (\*\*p < 0.05).

(H) A reduced GR-bound fraction over time (from  $49.7\% \pm 0.95\%$  to  $41\% \pm 0.89\%$ ) was responsible for the reduced burst frequency. The percentage of the bound fraction was derived from time lapses collected on a HILO microscope at a rate of 5 Hz with a 10-ms exposure time. Student's t test was performed to calculate p values (\*\*p < 0.05).

(I and J) Schematics illustrating the relationship between GR dwell times and burst length (I), as well as the proportion of bound GR molecules and the burst frequency (J).

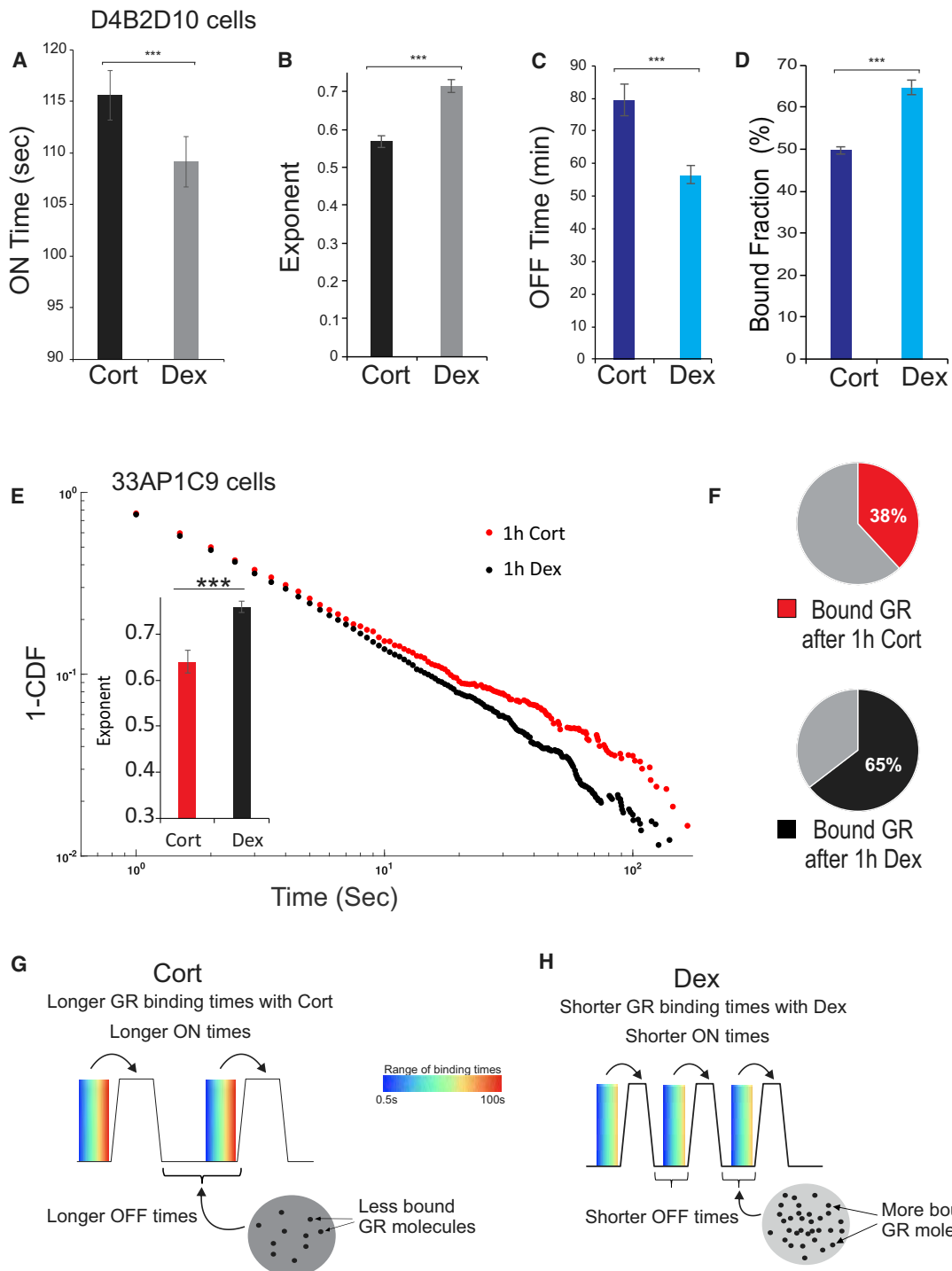


**Figure 5. Ligand-Specific Changes in Burst Frequency and Duration Are Associated with Ligand-Specific Changes in GR Dynamics**

(A and B) A comparison of burst length (ON time) after 1 h of treatment with Cort and Dex revealed that the (simple) bursts were longer upon Cort treatment ( $115.6 \pm 2.4$  s versus  $109.14 \pm 2.45$  s) (A) and associated with an increased GR dwell time and a reduced power law exponent ( $0.57 \pm 0.02$  versus  $0.72 \pm 0.02$ ) (B). (C) The OFF time (measured for the first 6 h of activation) was, however, shorter after Dex treatment ( $49.7 \pm 2.7$  min versus  $42.5 \pm 2.1$  min). (D) This correlated with the higher fraction of bound molecules found in Dex-treated nuclei ( $64.6\% \pm 1.75\%$ ) in comparison with the bound fraction found in Cort-treated nuclei ( $49.7\% \pm 0.95\%$ ). Student's t test was performed to calculate p values (\*\*p < 0.05).

(legend continued on next page)

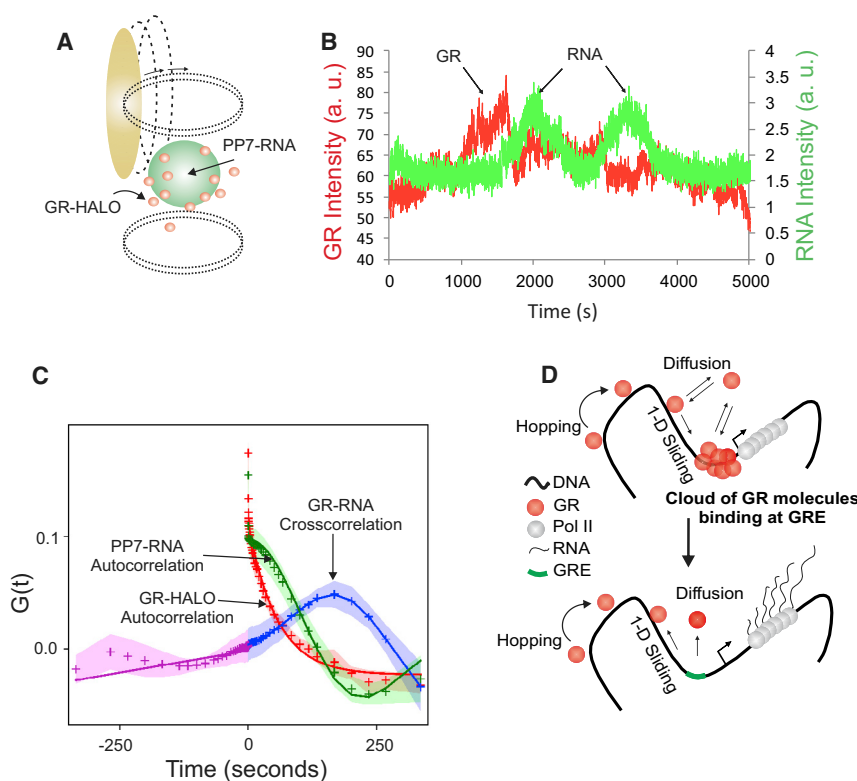


**Figure 6. A Direct Relationship between GR Binding and RNA Synthesis**

(A) A schematic of the 3DOT approach. The HALO-tagged GR molecules are shown in red, and the active TS is shown in green. A laser beam (represented by the yellow ellipse) traced four circular orbits surrounding the TS in two z planes above and below the locus (see STAR Methods for details).

(B) Representative intensity profiles of the RNA (green) and the GR (red) over time revealed the appearance of GR peaks preceding RNA synthesis.

(C) The autocorrelation analyses and the fitting of the data suggested an average GR binding time of  $56 \pm 5.2$  s and an average RNA dwell time of  $156 \pm 5.5$  s. In an agreement with the assumption that GR binding leads to RNA synthesis (Figure S6B), we obtained a positive red (GR) to green (RNA) cross-correlation (blue curve). The right shift of the center of the cross-correlation curve reflected an approximately 3-min delay ( $182 \pm 1.4$  s) between these two events.

(D) A schematic representation of GR binding to the MMTV GRE as a part of a cluster (a higher-order GR assembly) and recruitment of multiple RNA polymerase II (Pol II) molecules, a convoy of RNA polymerases (Tantale et al., 2016). The GR cluster disassembles either before or shortly after the beginning of elongation.

### Co-bursting of TSs

While examining the time lapses, we observed that the activity of the TSs within the same nucleus were sometimes coordinated (Figure 7A; Video S5), and we sought to quantify the occurrence of co-bursting in relation to the spatial proximity of the TSs. Cross-correlation analysis of TSs from Dex-treated 33AP1C9 cells revealed increased co-bursting for TSs closer than 2  $\mu\text{m}$  (Figure S7A). Unexpectedly, a second population of co-bursting TSs, which were separated by distances comparable with the diameter of the nuclei, was also apparent. Because 33AP1C9 cells are heterogeneous (Figure S7B), the distance between the TSs was normalized to the diameter of the corresponding nuclei (Figure 7B). To establish the empirical null distribution, we calculated the correlation between pairs of TSs from different cells ( $n = 200$  pairs) and showed that it has a mean correlation of 0 with a standard deviation of 0.13 (Figures S7C and S7D). Pairs of TSs that exhibited a correlation value greater than the 99th percentile value of the empirical null (0.338) (dotted line in Figure 7B) were significantly correlated. We found that 12 of 63 distal pairs of TSs (inter-site distance more than 0.5 times the normalized distance; Figure 7B, gray shading) were significantly correlated. The same comparison was performed for proximal TSs (inter-site distance less than 0.5 times the normalized dis-

tance), and we found that 7 of 13 of these pairs were significantly correlated. The binned data shown in Figure S7E were used to generate the exponential fit, which was superimposed on the un-binned data presented in Figure 7B (solid red line). This fit well describes the behavior of the pairs of TSs with an inter-site distance more than 0.5 of the normalized distance and was used to characterize the length scale at which the proximal co-bursting occurs (<2  $\mu\text{m}$ ). The binned data were also used to generate the contour plot shown in Figure 7C. A linear fit of the data presented in Figure S7E, with omission of the points corresponding to the proximal co-bursting, showed a deviation of the slope from 0 (a slope of 0.22), confirming the positive cross-correlation with distance (Figure S7F). As shown in Figure S7G, the peak of the cross-correlation function happens at time lag 0, indicating that no substantial cross-correlation delays between the co-bursting TSs are detectable. A representative nucleus exhibiting co-bursting of proximal and distal TSs and the corresponding RNA intensity traces are shown in Figure 7D and Figures 7E–7G, respectively. Although TS1 in Figure 7E is distal to TS2 and TS3, their transcriptional activities are largely correlated (Figure 7E–7G; Video S6). Additional experiments using D4B2D10 cells also confirmed the proximal and distal co-bursting of TSs (Figures S7H and S7I). Although the co-bursting of nearby TSs

(E) SMT experiments with 33AP1C9 cells also revealed increased dwell times (lower exponent) with Cort treatment in comparison with Dex treatment ( $0.64 \pm 0.03$  versus  $0.76 \pm 0.01$ , respectively). Student's t test was performed to calculate p values (\*\* $p < 0.05$ ).

(F) The smaller fraction of GR-bound molecules in 33AP1C9 cells treated with Cort in comparison with the Dex-treated cells ( $38.1\% \pm 1.1\%$  versus  $58.5\% \pm 1.4\%$ , respectively) is in an agreement with the longer OFF periods upon Cort treatment (Figure 2G).

(G and H) Schematic presentations of the ligand-specific differences in GR dwell time and bound fractions (G), as well as in burst duration and frequency (H).

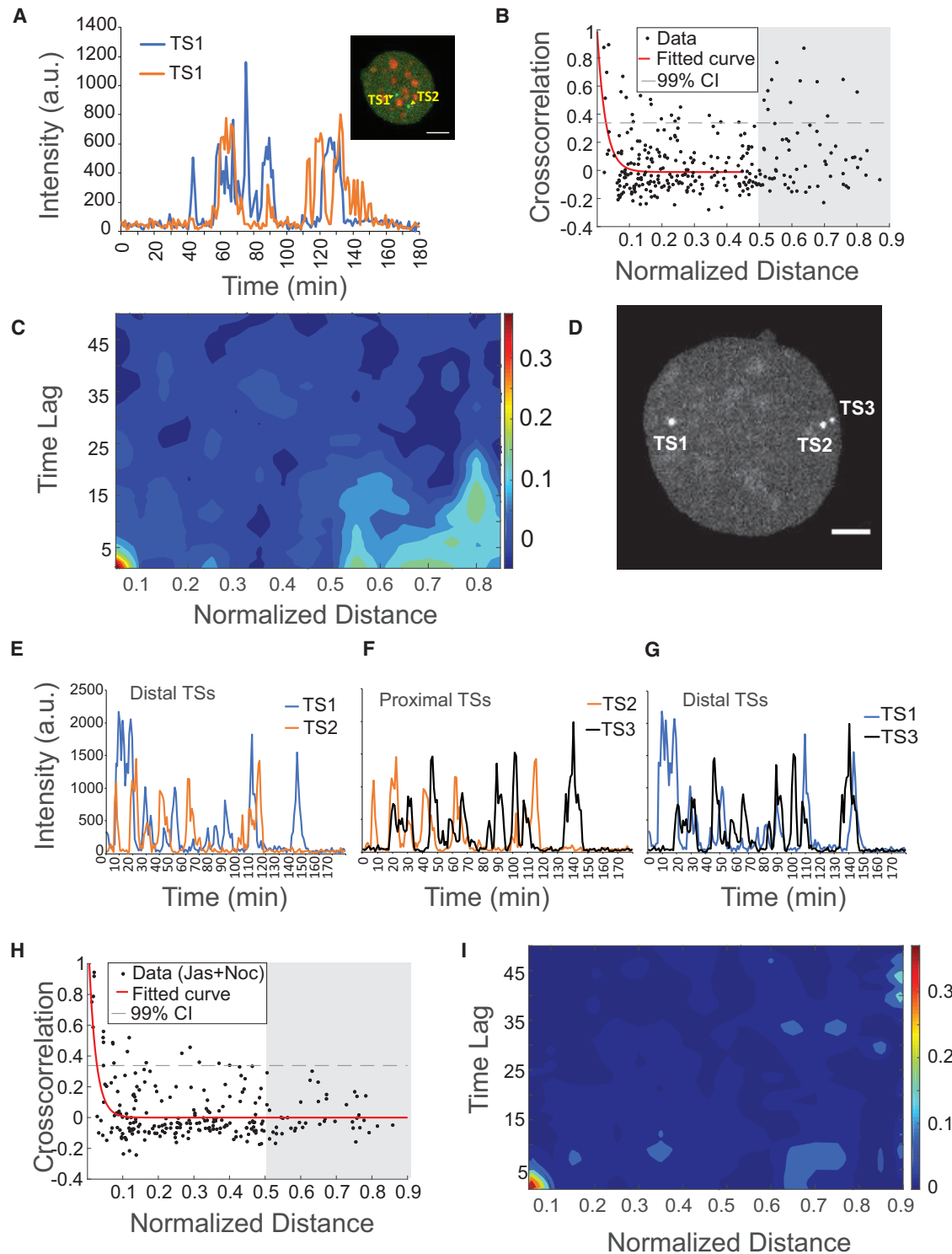


**Figure 7. Transcriptional Co-bursting at Proximal and Distal TSs**

(A) RNA intensity traces from two co-bursting TSs from the nucleus depicted in the inset (derived from [Video S5](#)).

(B) Cross-correlation analysis of paired TSs in conjunction to their proximity reveals a bimodal pattern in addition to the high cross-correlation at a short distance (red fitted curve); cross-correlation also increases when the paired TSs are near the nuclear periphery (gray shading). Data are derived from over 400 intensity traces from 3-h time-lapse videos acquired with 1-min resolution. Presented are unbinned data, and the dotted horizontal line corresponds to the 99th percentile of the empirical null distribution for the correlation (0.338) ([Figures S7C and S7D](#)).

(legend continued on next page)

could be explained by a shared microenvironment, the mechanisms of the distal co-bursting is harder to anticipate. The large distances between these co-bursting TSs makes the possibility of shared biochemical stimuli unlikely. Thus, we speculated that their activity could be coordinated through physical and/or mechanical forces. Arguably, the biggest contributors to mechanosensing and intracellular rheology are the nuclear envelope and the cytoskeletal network (Kirby and Lammerding, 2018; Mathieu and Manneville, 2019). We used a combination of nocodazole and jasplakinolide (Noc+Jas) to inhibit microtubule dynamics and actin disassembly, respectively, which abrogated the transmission of mechanical signals (Hui et al., 2015; Hui and Upadhyaya, 2017). Consistent with the idea that distal co-bursting may be a result of shared mechanical stimuli, the treatment perturbed the co-bursting of the distal TSs, whereas proximal co-bursting was unaffected (Figures 7H and 7I; Figure S7J). GR translocation to the nucleus was only slightly affected by this treatment (Figures S7K and S7L). We concluded that both the local microenvironment and mechanical coupling via the cytoskeleton coordinate the transcriptional activity of individual TSs.

## DISCUSSION

Here we used a GR-regulated promoter-reporter (MMTV-PP7), integrated at multiple locations in the genome of mouse cells expressing either endogenous or HALO-tagged GR, to study the real-time dynamics of individual GR molecules in relation to RNA synthesis. We developed and utilized a high-throughput analysis pipeline and uncovered distinct, treatment-specific bursting patterns.

Ultradian stimulation resulted in “restricted” RNA bursting confined to the duration of the hormonal pulse (Figures 2I and 2J). Averaging the intensity of over 100 traces recreated the previously observed gene pulsing (Stavreva et al., 2009; Figure 1B). In contrast, continuous hormone stimulation revealed an unrestricted RNA bursting pattern (Figure 2D). MMTV promoter invariably underwent time-dependent transcription downregulation (Hager et al., 2006; Voss et al., 2009) that lasted for several days (Figure 1E). The overall level of GR was reduced by 40% after 12 h of hormone stimulation (Figures S3E and S3F), and GR interactions with GREs, as measured by SMT, were diminished (Figure 4F). Moreover, transcription downregulation could also be related to the interplay between GR signaling and the circadian cycle (Lamia et al., 2011). Under normal physiological conditions, ultradian pulses are nested within the circadian cycle (Veldhuis et al., 1989). GCs cooperate with the circadian cycle by activating the Per1 gene (Figure 1J), which, together with

CRY1/2, is a part of the negative arm of the transcription-translation negative feedback loop of the cycle (Vitaterna et al., 1999). GCs also help to synchronize peripheral clocks with the central clock of the suprachiasmatic nucleus (SCN) (Nicolaides et al., 2014; Schibler et al., 2015). At the end of the active phase, ultradian pulses taper off, allowing the circadian cycle to continue unperturbed (Figure 1J). Prolonged GC treatment was, however, associated with an overproduction of the Per1 protein (Figure 1J), which perturbs the circadian cycle (Koyanagi et al., 2006).

The fact that hormone withdrawal restored the circadian cycle (Figure 1J) and that MMTV downregulation was alleviated by introduction of a hormone-free period (Figure 1I) suggests that hormone withdrawal was also required for proper GR target gene re-stimulation. Thus, the interplay between the circadian cycle and GC secretion is complex, and GC withdrawal is required for execution of the circadian cycle as well as for reactivation of GR target genes. Consistent with this finding, a lack of a difference between the morning and evening levels of GCs has been correlated with negative health outcomes (De Bacquer et al., 2009; Plat et al., 1999).

Using single-molecule tracking of individual GR molecules, we discovered a time-dependent reduction in GR dwell times as well as in the fraction of bound receptors (Figures 4F and 4G). These changes led to reductions in both the length and the frequency of RNA bursting (Figures 4B, 4C, and 4G).

Previous studies have correlated longer TF residence time with an overall higher transcriptional output (Gorski et al., 2008; Loffreda et al., 2017; Paakinaho et al., 2017; Rullan et al., 2018; Senecal et al., 2014; Stavreva et al., 2004). Our work, however, revealed a more complex relationship between these phenomena. A longer residence time (as found for Cort) was indeed related to a larger burst size; nevertheless, we found that the overall transcriptional output was higher with Dex than with Cort (Figure 2H), which correlated with a higher bound fraction of the GR with Dex. Considering that Dex treatment was associated with a shorter OFF time (more frequent bursting), we concluded that the transcriptional output in this system was regulated by varying the OFF time rather than the ON time.

We employed 3DOT microscopy to simultaneously measure the intensity of the GR and RNA in the same locus and to correlate their fluctuations over time (Figure 6A). Using autocorrelation analyses (Figure 6C), we estimated the average GR dwell time at the TS to be ~1 min; however, further experiments are required to ascribe a proper biological meaning to this number. The binding time measured for individual GR molecules was much shorter than the length of the average RNA burst (which, for D4B2D10 cells under Dex stimulation, ranged between 1.5–9.5 min) and insufficient to support the loading of multiple polymerases

(C) A contour plot in which the distance and the time lag are plotted on the x and y axes, respectively, and the collapsed z axis represents the degree of cross-correlation (derived from the binned data presented in Figure S7E). The contour plot shows co-bursting at both short and large distances.

(D) A representative image of a nucleus from a 33AP1C9 cell showing proximal (TS2 and TS3) and distal TSs (TS1 versus TS2 and TS3). This image was derived from the time lapse presented in Video S6 (frame 21), and only the PCP-GFP intensity is shown. Scale bar, 5 μm.

(E–G) Corresponding intensity traces of TS1 (E), TS2 (F), and TS3 (G).

(H) Treatment of cells with Noc+Jas selectively abrogated co-bursting of distal TSs (gray shading), whereas the high cross-correlation at a short inter-site distance (red fitted curve) was largely unaffected.

(I) A contour plot of the binned data (presented in Figure S7J), showing co-bursting of proximal transcription and a loss of co-bursting of distal TSs upon treatment with Noc+Jas.

creating the burst (Tantale et al., 2016). Thus, our data were inconsistent with a simple “one TF molecule per one burst” model, and alternative explanations of the results must be considered. Recent studies have shown that, in addition to forming homodimers, the GR can also form tetramers (Presman et al., 2016; Presman and Hager, 2017). Similar to other nuclear receptors, the GR has an intrinsically disordered N-terminal AF-1 domain, and such domains are capable of forming higher-order signaling assemblies (Shin and Brangwynne, 2017). In fact, nuclear “GR foci” are readily observable upon treatment with GCs (Stortz et al., 2017). In addition, the GR intensity peaks recorded by 3DOT clearly represented binding of multiple receptors (Figure 6B; Figure S6A). Therefore, it is likely that *MMTV* activation is a result of the simultaneous action of multiple GR molecules. Several earlier studies have proposed that clustering or phase separation of nuclear factors is important for transcription (Cho et al., 2016; Hnisz et al., 2017; Lu et al., 2018). Individual GR molecules within the “GR cloud” (Figure 6D) would still be mobile and exchange with the nuclear GR pool. Indeed, it has been shown recently that, in embryonic cells, the Mediator complex forms small transient and large stable clusters in which the individual Mediator molecules are dynamic (Cho et al., 2018). The lifetime of the GR clusters is likely to determine the length of the burst; however, the stability of such clusters would depend on the dwell time of individual GR molecules. Thus, indirectly, GR binding time will determine the length of the burst. Importantly, cross-correlation analysis of the recorded GR and RNA intensities revealed that the two events were temporally correlated and that GR binding preceded RNA synthesis by ~3 min (Figure 6C). This likely represents the multiple steps and combinatorial processes taking place between the initial GR binding and RNA synthesis. This also suggests that, by the time the RNA is observable, the initiating GR molecules have already dissociated from the promoter (Figure 6D). Whether this is a feature of *MMTV* promoter regulation or whether it represents a general phenomenon in mammalian gene regulation remains to be determined.

Finally, we discovered that the activity of individual TSs within the same nucleus could be coordinated. By exploring the relationship between this coordinated activation and the spatial proximity of the TSs, we discovered that closely spaced ( $\leq 2 \mu\text{m}$ ) TSs were more likely to co-burst (Figures 7B and 7C). Similar coordinated activity of adjacent TS has been reported earlier (Fukaya et al., 2016; Raj et al., 2006) and could reflect a shared local microenvironment. However, we also observed striking coordinated activity of distal TSs situated near the nuclear periphery (Figures 7B–7D). The co-bursting of distal TSs was unlikely to be a result of shared biochemical cues. Such signal(s) would also activate TSs located in the nuclear interior, which was not observed. We concluded that this coordination was most probably achieved through physical/mechanical cues transmitted by the cytoskeleton and the nuclear envelope. The cell nucleus is a major mechanosensing organelle, and the elements of the nuclear envelope connect the cytoskeleton and chromatin (Kirby and Lammerding, 2018; Mathieu and Manneville, 2019). We reasoned that if physical forces coordinated the activity of the distal TSs, then we could disrupt this process by interfering with the integrity of the cytoskeleton. By using small-molecule inhibitors that stabilize the cyto-

skeleton and inhibit force generation in cells (Hui et al., 2015; Hui and Upadhyaya, 2017), we selectively affected the co-bursting of distal TSs without interfering with the co-bursting of proximal TSs (Figures 7H and 7I). This coordination of the transcriptional activity of GR-regulated target promoters over large distances might represent a novel regulatory mechanism in GR signaling, and further studies will be required to understand this phenomenon.

In conclusion, we have implemented a high-throughput imaging platform in combination with state-of-the-art single-molecule imaging and analysis to correlate GR binding dynamics with real-time RNA synthesis at individual GR-regulated TSs. Together, our data demonstrate that the circadian cycle and the hormone release pattern (ultradian or constant) cooperate and sometimes antagonize each other to regulate GR activity and, ultimately, the kinetics of transcriptional bursting. By relating the GR binding pattern to burst size and frequency, we provide a mechanistic insight into mammalian gene regulation.

## STAR★METHODS

Detailed methods are provided in the online version of this paper and include the following:

- **KEY RESOURCES TABLE**
- **LEAD CONTACT AND MATERIALS AVAILABILITY**
- **EXPERIMENTAL MODEL AND SUBJECT DETAILS**
  - Plasmids and cell lines
- **METHOD DETAILS**
  - Zeiss LSM780 life cell imaging of TSs
  - Manual tracking of TSs
  - GFP-GR translocation experiments
  - Immunostaining
  - Automated analysis of nuclear and cytoplasmic fluorescence
  - Concentration- and time-dependent induction of TSs
  - smRNA FISH experiments
  - Yokogawa CV7000 live cells imaging conditions
  - Long-term Induction experiments
  - Hormone withdrawal experiments
  - Ultradian life cell experiments
  - Yokogawa CV7000 high-throughput data processing
  - Single molecule tracking (SMT) Experiments
  - Western blot analyses
  - GR chromatin immunoprecipitation (ChIP) and ChIP-seq
  - Gene expression studies by RT-qPCR
  - Orbital tracking
  - Characterization of burst ON times by autocorrelation analysis
  - Co-bursting analysis
- **QUANTIFICATION AND STATISTICAL ANALYSIS**
- **DATA AND CODE AVAILABILITY**

## SUPPLEMENTAL INFORMATION

Supplemental Information can be found online at <https://doi.org/10.1016/j.molcel.2019.06.042>.

## ACKNOWLEDGMENTS

We thank Tatiana Karpova and David Ball (NCI) for assistance with imaging. We thank Luke Lavis (Janelia Research Campus) for providing HALO dyes and Katherine M. McKinnon from the NCI FACS Core Facility for sorting the cells. We thank Daniel Larson (NCI) for critically reading the manuscript. We also thank Iain Sawyer (NCI) for critically reading and editing the manuscript. We thank Sohyoung Kim (NCI) for feedback on data analysis. We thank the CBIIT Server Team (NCI, NIH) and the High-Performance Computing Group (CIT, NIH) for computational hardware support. The study also utilized the high-performance computational resources of the NIH HPC Biowulf cluster (<https://hpc.nih.gov>). This research was supported (in part) by the Intramural Research Program of the NIH, NCI, and CCR. A.H. and M.L.F. were supported by the Research Corporation for Science Advancement and the Gordon and Betty Moore Foundation through grant GBMF5263.10 and by NIGMS through grant 1R15GM123446-01. A.U. acknowledges support from NSF PHY-1607645 and PHY-1806903 and the UMD/NCI Cancer Technology Partnership.

## AUTHOR CONTRIBUTIONS

D.A.S. and G.L.H. conceived the experiments and wrote the original draft with subsequent input and editing from all coauthors. D.A.S. performed most imaging experiments, analyzed data, and prepared figures. D.A.G. developed and implemented a novel SMT analysis method, performed extensive data analysis, designed experiments, and participated in all stages of manuscript preparation. G.F. performed and analyzed SMT experiments, contributed to the development of the SMT analysis, and participated in all stages of manuscript preparation. P.R.G., G.F.Z., and G.P. developed the high-throughput imaging and analysis pipeline, analyzed data, and helped with figure preparation. V.S. generated plasmids and performed confirmatory experiments. A.M. edited figures and performed western blot, ChIP, and circadian experiments. T.A.J. performed ChIP-seq experiments and data analysis. G.W. performed circadian experiments. A.H. performed 3DOT experiments and data analysis. M.L.F. provided valuable expertise for 3DOT experimentation and data analysis and contributed to manuscript preparation. D.M.P. contributed to the development of the SMT analysis. M.P. provided reagents and expertise. R.L.S. developed the GR-HALO cell lines. A.U. supervised the development of the SMT analysis method, supervised data analysis, and participated in manuscript preparation. G.L.H. supervised the project.

## DECLARATION OF INTERESTS

The authors declare no competing interests.

Received: November 15, 2018

Revised: February 7, 2019

Accepted: June 26, 2019

Published: August 14, 2019

## REFERENCES

- Annibale, P., and Gratton, E. (2015). Single cell visualization of transcription kinetics variance of highly mobile identical genes using 3D nanoimaging. *Sci. Rep.* **5**, 9258.
- Aulinas, A., and Webb, S.M. (2014). Health-related quality of life in primary and secondary adrenal insufficiency. *Expert Rev. Pharmacoecon. Outcomes Res.* **14**, 873–888.
- Bahar Halpern, K., Tanami, S., Landen, S., Chapal, M., Szlak, L., Hutzler, A., Nizhberg, A., and Itzkovitz, S. (2015). Bursty gene expression in the intact mammalian liver. *Mol. Cell* **58**, 147–156.
- Ball, D.A., Mehta, G.D., Salomon-Kent, R., Mazza, D., Morisaki, T., Mueller, F., McNally, J.G., and Karpova, T.S. (2016). Single molecule tracking of Ace1p in *Saccharomyces cerevisiae* defines a characteristic residence time for non-specific interactions of transcription factors with chromatin. *Nucleic Acids Res.* **44**, e160.
- Balsalobre, A., Brown, S.A., Marcacci, L., Tronche, F., Kellendonk, C., Reichardt, H.M., Schütz, G., and Schibler, U. (2000). Resetting of circadian time in peripheral tissues by glucocorticoid signaling. *Science* **289**, 2344–2347.
- Bartman, C.R., Hsu, S.C., Hsiung, C.C., Raj, A., and Blobel, G.A. (2016). Enhancer Regulation of Transcriptional Bursting Parameters Revealed by Forced Chromatin Looping. *Mol. Cell* **62**, 237–247.
- Bengtsson, M., Ståhlberg, A., Rorsman, P., and Kubista, M. (2005). Gene expression profiling in single cells from the pancreatic islets of Langerhans reveals lognormal distribution of mRNA levels. *Genome Res.* **15**, 1388–1392.
- Benzinger, D., and Khammash, M. (2018). Pulsatile inputs achieve tunable attenuation of gene expression variability and graded multi-gene regulation. *Nat. Commun.* **9**, 3521.
- Berthold, M.R., Cebron, N., Dill, F., Gabriel, T.R., Kötter, T., Meinl, T., Ohl, P., Sieb, C., Thiel, K., and Wiswedel, B. (2008). KNIME: The Konstanz Information Miner. In *Data Analysis, Machine Learning and Applications. Studies in Classification, Data Analysis, and Knowledge Organization*, C. Preisach, H. Burkhardt, I. Schmidt-Thieme, and R. Decker, eds. (Springer), pp. 319–326.
- Box, G.E.P., Jenkins, G.M., and Reinsel, G.C. (1994). *Time Series Analysis Forecasting and Control*, Third Edition (Prentice Hall).
- Breiman, L. (2001). Random Forests. *Mach. Learn.* **45**, 5–32.
- Cai, L., Dalal, C.K., and Elowitz, M.B. (2008). Frequency-modulated nuclear localization bursts coordinate gene regulation. *Nature* **455**, 485–490.
- Chao, J.A., Patskovsky, Y., Almo, S.C., and Singer, R.H. (2008). Structural basis for the coevolution of a viral RNA-protein complex. *Nat. Struct. Mol. Biol.* **15**, 103–105.
- Chen, J., Zhang, Z., Li, L., Chen, B.C., Revyakin, A., Hajj, B., Legant, W., Dahan, M., Lionnet, T., Betzig, E., et al. (2014). Single-molecule dynamics of enhanceosome assembly in embryonic stem cells. *Cell* **156**, 1274–1285.
- Cho, W.K., Jayanth, N., English, B.P., Inoue, T., Andrews, J.O., Conway, W., Grimm, J.B., Spille, J.H., Lavis, L.D., Lionnet, T., and Cisse, I.I. (2016). RNA Polymerase II cluster dynamics predict mRNA output in living cells. *eLife* **5**, e13617.
- Cho, W.K., Spille, J.H., Hecht, M., Lee, C., Li, C., Grube, V., and Cisse, I.I. (2018). Mediator and RNA polymerase II clusters associate in transcription-dependent condensates. *Science* **361**, 412–415.
- Chubb, J.R., Trcek, T., Shenoy, S.M., and Singer, R.H. (2006). Transcriptional pulsing of a developmental gene. *Curr. Biol.* **16**, 1018–1025.
- Conway-Campbell, B.L., Sarabdjitsingh, R.A., McKenna, M.A., Pooley, J.R., Kershaw, Y.M., Meijer, O.C., de Kloet, E.R., and Lightman, S.L. (2010). Glucocorticoid ultradian rhythmicity directs cyclical gene pulsing of the clock gene period 1 in rat hippocampus. *J. Neuroendocrinol.* **22**, 1093–1100.
- Corrigan, A.M., and Chubb, J.R. (2014). Regulation of transcriptional bursting by a naturally oscillating signal. *Curr. Biol.* **24**, 205–211.
- Crocker, J.C., and Grier, D.G. (1996). Methods of digital video microscopy for colloidal studies. *J. Colloid. Interface Sci.* **179**, 298–310.
- Dar, R.D., Razooky, B.S., Singh, A., Trimeloni, T.V., McCollum, J.M., Cox, C.D., Simpson, M.L., and Weinberger, L.S. (2012). Transcriptional burst frequency and burst size are equally modulated across the human genome. *Proc. Natl. Acad. Sci. USA* **109**, 17454–17459.
- De Bacquer, D., Van Rissegem, M., Clays, E., Kittel, F., De Backer, G., and Braeckman, L. (2009). Rotating shift work and the metabolic syndrome: a prospective study. *Int. J. Epidemiol.* **38**, 848–854.
- Dietz, C., and Berthold, M.R. (2016). KNIME for Open-Source Bioimage Analysis: A Tutorial. *Adv. Anat. Embryol. Cell Biol.* **219**, 179–197.
- Donovan, B.T., Huynh, A., Ball, D.A., Patel, H.P., Poirier, M.G., Larson, D.R., Ferguson, M.L., and Lenstra, T.L. (2019). Live-cell imaging reveals the interplay between transcription factors, nucleosomes, and bursting. *EMBO J.* **38**, e100809.
- Droste, S.K., de Groot, L., Atkinson, H.C., Lightman, S.L., Reul, J.M., and Linthorst, A.C. (2008). Corticosterone levels in the brain show a distinct

- ultradian rhythm but a delayed response to forced swim stress. *Endocrinology* 149, 3244–3253.
- Feeiders, R.A., Pulgar, S.J., Kempel, A., and Pereira, A.M. (2012). The burden of Cushing's disease: clinical and health-related quality of life aspects. *Eur. J. Endocrinol.* 167, 311–326.
- Ferguson, M.L., Le Coq, D., Jules, M., Aymerich, S., Radulescu, O., Declerck, N., and Royer, C.A. (2012). Reconciling molecular regulatory mechanisms with noise patterns of bacterial metabolic promoters in induced and repressed states. *Proc. Natl. Acad. Sci. USA* 109, 155–160.
- Fragoso, G., Pennie, W.D., John, S., and Hager, G.L. (1998). The position and length of the steroid-dependent hypersensitive region in the mouse mammary tumor virus long terminal repeat are invariant despite multiple nucleosome B frames. *Mol. Cell. Biol.* 18, 3633–3644.
- Fritzs, C., Baumgärtner, S., Kuban, M., Steinhorn, D., Reid, G., and Legewie, S. (2018). Estrogen-dependent control and cell-to-cell variability of transcriptional bursting. *Mol. Syst. Biol.* 14, e7678.
- Fukaya, T., Lim, B., and Levine, M. (2016). Enhancer Control of Transcriptional Bursting. *Cell* 166, 358–368.
- Garcia, D.A., Presman, D.M., Fettweis, G., Paakinaho, V., Jarsinski, C., Upadhyaya, A., and Hager, G.L. (2019). A new model for single-molecule tracking analysis of transcription factor dynamics. *bioRxiv*. <https://doi.org/10.1101/637355>.
- Gebhardt, J.C., Suter, D.M., Roy, R., Zhao, Z.W., Chapman, A.R., Basu, S., Maniatis, T., and Xie, X.S. (2013). Single-molecule imaging of transcription factor binding to DNA in live mammalian cells. *Nat. Methods* 10, 421–426.
- George, C.L., Birnie, M.T., Flynn, B.P., Kershaw, Y.M., Lightman, S.L., and Conway-Campbell, B.L. (2017). Ultradian glucocorticoid exposure directs gene-dependent and tissue-specific mRNA expression patterns *in vivo*. *Mol. Cell. Endocrinol.* 439, 46–53.
- Georgel, P.T., Fletcher, T.M., Hager, G.L., and Hansen, J.C. (2003). Formation of higher-order secondary and tertiary chromatin structures by genomic mouse mammary tumor virus promoters. *Genes Dev.* 17, 1617–1629.
- Golding, I., Paulsson, J., Zawilski, S.M., and Cox, E.C. (2005). Real-time kinetics of gene activity in individual bacteria. *Cell* 123, 1025–1036.
- Gorski, S.A., Snyder, S.K., John, S., Grummt, I., and Misteli, T. (2008). Modulation of RNA polymerase assembly dynamics in transcriptional regulation. *Mol. Cell* 30, 486–497.
- Grimm, J.B., English, B.P., Chen, J., Slaughter, J.P., Zhang, Z., Revyakin, A., Patel, R., Macklin, J.J., Normanno, D., Singer, R.H., et al. (2015). A general method to improve fluorophores for live-cell and single-molecule microscopy. *Nat. Methods* 12, 244–250, 3, 250.
- Grimm, J.B., English, B.P., Choi, H., Muthusamy, A.K., Mehl, B.P., Dong, P., Brown, T.A., Lippincott-Schwartz, J., Liu, Z., Lionnet, T., and Lavis, L.D. (2016). Bright photoactivatable fluorophores for single-molecule imaging. *Nat. Methods* 13, 985–988.
- Gudla, P.R., Nakayama, K., Pegoraro, G., and Misteli, T. (2017). SpotLearn: Convolutional Neural Network for Detection of Fluorescence In Situ Hybridization (FISH) Signals in High-Throughput Imaging Approaches. *Cold Spring Harb. Symp. Quant. Biol.* 82, 57–70.
- Hager, G.L., Elbi, C., Johnson, T.A., Voss, T., Nagaich, A.K., Schiltz, R.L., Qiu, Y., and John, S. (2006). Chromatin dynamics and the evolution of alternate promoter states. *Chromosome Res.* 14, 107–116.
- Hager, G.L., McNally, J.G., and Misteli, T. (2009). Transcription dynamics. *Mol. Cell* 35, 741–753.
- Heinz, S., Benner, C., Spann, N., Bertolino, E., Lin, Y.C., Laslo, P., Cheng, J.X., Murre, C., Singh, H., and Glass, C.K. (2010). Simple combinations of lineage-determining transcription factors prime cis-regulatory elements required for macrophage and B cell identities. *Mol. Cell* 38, 576–589.
- Henley, D.E., Leendertz, J.A., Russell, G.M., Wood, S.A., Taheri, S., Woltersdorf, W.W., and Lightman, S.L. (2009). Development of an automated blood sampling system for use in humans. *J. Med. Eng. Technol.* 33, 199–208.
- Hnisz, D., Shrinivas, K., Young, R.A., Chakraborty, A.K., and Sharp, P.A. (2017). A Phase Separation Model for Transcriptional Control. *Cell* 169, 13–23.
- Hui, K.L., and Upadhyaya, A. (2017). Dynamic microtubules regulate cellular contractility during T-cell activation. *Proc. Natl. Acad. Sci. USA* 114, E4175–E4183.
- Hui, K.L., Balagopalan, L., Samelson, L.E., and Upadhyaya, A. (2015). Cytoskeletal forces during signaling activation in Jurkat T-cells. *Mol. Biol. Cell* 26, 685–695.
- Izeddin, I., Récamier, V., Bosanac, L., Cissé, I.I., Boudarene, L., Dugast-Darzacq, C., Proux, F., Bénichou, O., Voituriez, R., Bensaude, O., et al. (2014). Single-molecule tracking in live cells reveals distinct target-search strategies of transcription factors in the nucleus. *eLife* 3, e02230.
- Jaqaman, K., Loerke, D., Mettlen, M., Kuwata, H., Grinstein, S., Schmid, S.L., and Danuser, G. (2008). Robust single-particle tracking in live-cell time-lapse sequences. *Nat. Methods* 5, 695–702.
- John, S., Johnson, T.A., Sung, M.H., Biddie, S.C., Trump, S., Koch-Paiz, C.A., Davis, S.R., Walker, R., Meltzer, P.S., and Hager, G.L. (2009). Kinetic complexity of the global response to glucocorticoid receptor action. *Endocrinology* 150, 1766–1774.
- Jowhar, Z., Gudla, P.R., Shachar, S., Wangsa, D., Russ, J.L., Pegoraro, G., Ried, T., Raznahan, A., and Misteli, T. (2018a). HiCTMap: Detection and analysis of chromosome territory structure and position by high-throughput imaging. *Methods* 142, 30–38.
- Jowhar, Z., Shachar, S., Gudla, P.R., Wangsa, D., Torres, E., Russ, J.L., Pegoraro, G., Ried, T., Raznahan, A., and Misteli, T. (2018b). Effects of human sex chromosome dosage on spatial chromosome organization. *Mol. Biol. Cell* 29, 2458–2469.
- Kaplan, E.L., and Meier, P. (1958). Nonparametric estimation from incomplete observations. *J. Am. Stat. Assoc.* 53, 457–481.
- Kirby, T.J., and Lammerding, J. (2018). Emerging views of the nucleus as a cellular mechanosensor. *Nat. Cell Biol.* 20, 373–381.
- Kis-Petikova, K., and Gratton, E. (2004). Distance measurement by circular scanning of the excitation beam in the two-photon microscope. *Microsc. Res. Tech.* 63, 34–49.
- Kitagawa, H., Sugo, N., Morimatsu, M., Arai, Y., Yanagida, T., and Yamamoto, N. (2017). Activity-Dependent Dynamics of the Transcription Factor of cAMP-Response Element Binding Protein in Cortical Neurons Revealed by Single-Molecule Imaging. *J. Neurosci.* 37, 1–10.
- Ko, M.S., Nakauchi, H., and Takahashi, N. (1990). The dose dependence of glucocorticoid-inducible gene expression results from changes in the number of transcriptionally active templates. *EMBO J.* 9, 2835–2842.
- Koyanagi, S., Okazawa, S., Kuramoto, Y., Ushijima, K., Shimeno, H., Soeda, S., Okamura, H., and Ohdo, S. (2006). Chronic treatment with prednisolone represses the circadian oscillation of clock gene expression in mouse peripheral tissues. *Mol. Endocrinol.* 20, 573–583.
- Lamia, K.A., Papp, S.J., Yu, R.T., Barish, G.D., Uhlenhaut, N.H., Jonker, J.W., Downes, M., and Evans, R.M. (2011). Cryptochromes mediate rhythmic repression of the glucocorticoid receptor. *Nature* 480, 552–556.
- Larson, D.R., Zenklusen, D., Wu, B., Chao, J.A., and Singer, R.H. (2011). Real-time observation of transcription initiation and elongation on an endogenous yeast gene. *Science* 332, 475–478.
- Larson, D.R., Fritzs, C., Sun, L., Meng, X., Lawrence, D.S., and Singer, R.H. (2013). Direct observation of frequency modulated transcription in single cells using light activation. *eLife* 2, e00750.
- Legland, D., Arganda-Carreras, I., and Andrey, P. (2016). MorphoLibJ: integrated library and plugins for mathematical morphology with ImageJ. *Bioinformatics* 32, 3532–3534.
- Lenstra, T.L., Coulon, A., Chow, C.C., and Larson, D.R. (2015). Single-Molecule Imaging Reveals a Switch between Spurious and Functional ncRNA Transcription. *Mol. Cell* 60, 597–610.
- Levi, V., Ruan, Q., Kis-Petikova, K., and Gratton, E. (2003). Scanning FCS, a novel method for three-dimensional particle tracking. *Biochem. Soc. Trans.* 31, 997–1000.

- Levi, V., Ruan, Q., and Gratton, E. (2005a). 3-D particle tracking in a two-photon microscope: application to the study of molecular dynamics in cells. *Biophys. J.* 88, 2919–2928.
- Levi, V., Ruan, Q., Plutz, M., Belmont, A.S., and Gratton, E. (2005b). Chromatin dynamics in interphase cells revealed by tracking in a two-photon excitation microscope. *Biophys. J.* 89, 4275–4285.
- Levine, J.H., Lin, Y., and Elowitz, M.B. (2013). Functional roles of pulsing in genetic circuits. *Science* 342, 1193–1200.
- Lightman, S.L., Wiles, C.C., Atkinson, H.C., Henley, D.E., Russell, G.M., Leendertz, J.A., McKenna, M.A., Spiga, F., Wood, S.A., and Conway-Campbell, B.L. (2008). The significance of glucocorticoid pulsatility. *Eur. J. Pharmacol.* 583, 255–262.
- Loffreda, A., Jacchetti, E., Antunes, S., Rainone, P., Daniele, T., Morisaki, T., Bianchi, M.E., Tacchetti, C., and Mazza, D. (2017). Live-cell p53 single-molecule binding is modulated by C-terminal acetylation and correlates with transcriptional activity. *Nat. Commun.* 8, 313.
- Lu, H., Yu, D., Hansen, A.S., Ganguly, S., Liu, R., Heckert, A., Darzacq, X., and Zhou, Q. (2018). Phase-separation mechanism for C-terminal hyperphosphorylation of RNA polymerase II. *Nature* 558, 318–323.
- Lukinavičius, G., Blaukopf, C., Pershagen, E., Schena, A., Reymond, L., Derivery, E., Gonzalez-Gaitan, M., D'Este, E., Hell, S.W., Wolfram Gerlich, D., and Johnsson, K. (2015). SiR-Hoechst is a far-red DNA stain for live-cell nanoscopy. *Nat. Commun.* 6, 8497.
- Mathieu, S., and Manneville, J.B. (2019). Intracellular mechanics: connecting rheology and mechanotransduction. *Curr. Opin. Cell Biol.* 56, 34–44.
- Mazza, D., Abernathy, A., Golob, N., Morisaki, T., and McNally, J.G. (2012). A benchmark for chromatin binding measurements in live cells. *Nucleic Acids Res.* 40, e119.
- Mazza, D., Ganguly, S., and McNally, J.G. (2013). Monitoring dynamic binding of chromatin proteins in vivo by single-molecule tracking. *Methods Mol. Biol.* 1042, 117–137.
- McMaster, A., Jangani, M., Sommer, P., Han, N., Brass, A., Beesley, S., Lu, W., Berry, A., Loudon, A., Donn, R., and Ray, D.W. (2011). Ultradian cortisol pulsatility encodes a distinct, biologically important signal. *PLoS ONE* 6, e15766.
- Migeon, C.J., Tyler, F.H., Mahoney, J.P., Florentin, A.A., Castle, H., Bliss, E.L., and Samuels, L.T. (1956). The diurnal variation of plasma levels and urinary excretion on 17-hydroxycorticosteroids in normal subjects, night workers and blind subjects. *J. Clin. Endocrinol. Metab.* 16, 622–633.
- Molina, N., Suter, D.M., Cannavo, R., Zoller, B., Gotic, I., and Naef, F. (2013). Stimulus-induced modulation of transcriptional bursting in a single mammalian gene. *Proc. Natl. Acad. Sci. USA* 110, 20563–20568.
- Morisaki, T., Müller, W.G., Golob, N., Mazza, D., and McNally, J.G. (2014). Single-molecule analysis of transcription factor binding at transcription sites in live cells. *Nat. Commun.* 5, 4456.
- Newville, M., Stensitzki, T., Allen, D.B., and Ingargiola, A. (2014). LMFIT: Non-linear least-square minimization and curve-fitting for python (Zenodo).
- Nicolaides, N.C., Charmandari, E., Chrousos, G.P., and Kino, T. (2014). Circadian endocrine rhythms: the hypothalamic-pituitary-adrenal axis and its actions. *Ann. N Y Acad. Sci.* 1318, 71–80.
- Nicolas, D., Zoller, B., Suter, D.M., and Naef, F. (2018). Modulation of transcriptional burst frequency by histone acetylation. *Proc. Natl. Acad. Sci. USA* 115, 7153–7158.
- Nieman, L.K., and Ilias, I. (2005). Evaluation and treatment of Cushing's syndrome. *Am. J. Med.* 118, 1340–1346.
- Normanno, D., Dahan, M., and Darzacq, X. (2012). Intra-nuclear mobility and target search mechanisms of transcription factors: a single-molecule perspective on gene expression. *Biochim. Biophys. Acta* 1819, 482–493.
- Ono, D., Honma, K., and Honma, S. (2015). Circadian and ultradian rhythms of clock gene expression in the suprachiasmatic nucleus of freely moving mice. *Sci. Rep.* 5, 12310.
- Otsu, N. (1979). A threshold selection method from gray-level histograms. *IEEE Trans. Syst. Man Cybern.* 9, 62–66.
- Paakinaho, V., Presman, D.M., Ball, D.A., Johnson, T.A., Schiltz, R.L., Levitt, P., Mazza, D., Morisaki, T., Karpova, T.S., and Hager, G.L. (2017). Single-molecule analysis of steroid receptor and cofactor action in living cells. *Nat. Commun.* 8, 15896.
- Palangat, M., and Larson, D.R. (2016). Single-gene dual-color reporter cell line to analyze RNA synthesis in vivo. *Methods* 103, 77–85.
- Paré, A., Lemons, D., Kosman, D., Beaver, W., Freund, Y., and McGinnis, W. (2009). Visualization of individual Scr mRNAs during *Drosophila* embryogenesis yields evidence for transcriptional bursting. *Curr. Biol.* 19, 2037–2042.
- Pinidiyaarachchi, A., and Wählby, C. (2005). Seeded Watersheds for Combined Segmentation and Tracking of Cells. In *Image Analysis and Processing – ICIAP 2005 Lecture Notes in Computer Science*, vol. 3617, F. Roli and S. Vitulano, eds. (Springer), pp. 336–343.
- Plat, L., Leproult, R., L'Hermite-Baleriaux, M., Fery, F., Mockel, J., Polonsky, K.S., and Van Cauter, E. (1999). Metabolic effects of short-term elevations of plasma cortisol are more pronounced in the evening than in the morning. *J. Clin. Endocrinol. Metab.* 84, 3082–3092.
- Presman, D.M., and Hager, G.L. (2017). More than meets the dimer: What is the quaternary structure of the glucocorticoid receptor? *Transcription* 8, 32–39.
- Presman, D.M., Ganguly, S., Schiltz, R.L., Johnson, T.A., Karpova, T.S., and Hager, G.L. (2016). DNA binding triggers tetramerization of the glucocorticoid receptor in live cells. *Proc. Natl. Acad. Sci. USA* 113, 8236–8241.
- Presman, D.M., Ball, D.A., Paakinaho, V., Grimm, J.B., Lavis, L.D., Karpova, T.S., and Hager, G.L. (2017). Quantifying transcription factor binding dynamics at the single-molecule level in live cells. *Methods* 123, 76–88.
- Raj, A., Peskin, C.S., Tranchina, D., Vargas, D.Y., and Tyagi, S. (2006). Stochastic mRNA synthesis in mammalian cells. *PLoS Biol.* 4, e309.
- Raj, A., Rifkin, S.A., Andersen, E., and van Oudenaarden, A. (2010). Variability in gene expression underlies incomplete penetrance. *Nature* 463, 913–918.
- Rodriguez, J., Ren, G., Day, C.R., Zhao, K., Chow, C.C., and Larson, D.R. (2019). Intrinsic Dynamics of a Human Gene Reveal the Basis of Expression Heterogeneity. *Cell* 176, 213–226.e18.
- Roukos, V., Burgess, R.C., and Misteli, T. (2014). Generation of cell-based systems to visualize chromosome damage and translocations in living cells. *Nat. Protoc.* 9, 2476–2492.
- Rullan, M., Benzinger, D., Schmidt, G.W., Milias-Argeitis, A., and Khammash, M. (2018). An Optogenetic Platform for Real-Time, Single-Cell Interrogation of Stochastic Transcriptional Regulation. *Mol. Cell* 70, 745–756.e6.
- Russell, G.M., Kalafatakis, K., and Lightman, S.L. (2015). The importance of biological oscillators for hypothalamic-pituitary-adrenal activity and tissue glucocorticoid response: coordinating stress and neurobehavioural adaptation. *J. Neuroendocrinol.* 27, 378–388.
- Sander, J.D., and Joung, J.K. (2014). CRISPR-Cas systems for editing, regulating and targeting genomes. *Nat. Biotechnol.* 32, 347–355.
- Schibler, U., Gotic, I., Saini, C., Gos, P., Curie, T., Emmenegger, Y., Sinturel, F., Gosselin, P., Gerber, A., Fleury-Olela, F., et al. (2015). Clock-Talk: Interactions between Central and Peripheral Circadian Oscillators in Mammals. *Cold Spring Harb. Symp. Quant. Biol.* 80, 223–232.
- Schwille, P., Haupts, U., Maiti, S., and Webb, W.W. (1999). Molecular dynamics in living cells observed by fluorescence correlation spectroscopy with one- and two-photon excitation. *Biophys. J.* 77, 2251–2265.
- Seale, J.V., Wood, S.A., Atkinson, H.C., Bate, E., Lightman, S.L., Ingram, C.D., Jessop, D.S., and Harbuz, M.S. (2004). Gonadectomy reverses the sexually dimorphic patterns of circadian and stress-induced hypothalamic-pituitary-adrenal axis activity in male and female rats. *J. Neuroendocrinol.* 16, 516–524.
- Senecal, A., Munsky, B., Proux, F., Ly, N., Braye, F.E., Zimmer, C., Mueller, F., and Darzacq, X. (2014). Transcription factors modulate c-Fos transcriptional bursts. *Cell Rep.* 8, 75–83.
- Shin, Y., and Brangwynne, C.P. (2017). Liquid phase condensation in cell physiology and disease. *Science* 357, eaaf4382.

- Soille, P. (2013). Morphological Image Analysis: Principles and Applications (Springer Science & Business Media).
- Speil, J., Baumgart, E., Siebrasse, J.P., Veith, R., Vinkemeier, U., and Kubitscheck, U. (2011). Activated STAT1 transcription factors conduct distinct saltatory movements in the cell nucleus. *Biophys. J.* 101, 2592–2600.
- Stavreva, D.A., Müller, W.G., Hager, G.L., Smith, C.L., and McNally, J.G. (2004). Rapid glucocorticoid receptor exchange at a promoter is coupled to transcription and regulated by chaperones and proteasomes. *Mol. Cell. Biol.* 24, 2682–2697.
- Stavreva, D.A., Wiench, M., John, S., Conway-Campbell, B.L., McKenna, M.A., Pooley, J.R., Johnson, T.A., Voss, T.C., Lightman, S.L., and Hager, G.L. (2009). Ultradian hormone stimulation induces glucocorticoid receptor-mediated pulses of gene transcription. *Nat. Cell Biol.* 11, 1093–1102.
- Stavreva, D.A., George, A.A., Klausmeyer, P., Varticovski, L., Sack, D., Voss, T.C., Schiltz, R.L., Blazer, V.S., Iwanowicz, L.R., and Hager, G.L. (2012a). Prevalent glucocorticoid and androgen activity in US water sources. *Sci. Rep.* 2, 937.
- Stavreva, D.A., Varticovski, L., and Hager, G.L. (2012b). Complex dynamics of transcription regulation. *Biochim. Biophys. Acta* 1819, 657–666.
- Stavreva, D.A., Coulon, A., Baek, S., Sung, M.H., John, S., Stixova, L., Tesikova, M., Hakim, O., Miranda, T., Hawkins, M., et al. (2015). Dynamics of chromatin accessibility and long-range interactions in response to glucocorticoid pulsing. *Genome Res.* 25, 845–857.
- Stortz, M., Presman, D.M., Bruno, L., Annibale, P., Dansey, M.V., Burton, G., Gratton, E., Pecci, A., and Levi, V. (2017). Mapping the Dynamics of the Glucocorticoid Receptor within the Nuclear Landscape. *Sci. Rep.* 7, 6219.
- Sugo, N., Morimatsu, M., Arai, Y., Kousoku, Y., Ohkuni, A., Nomura, T., Yanagida, T., and Yamamoto, N. (2015). Single-Molecule Imaging Reveals Dynamics of CREB Transcription Factor Bound to Its Target Sequence. *Sci. Rep.* 5, 10662.
- Suter, D.M., Molina, N., Gatfield, D., Schneider, K., Schibler, U., and Naef, F. (2011a). Mammalian genes are transcribed with widely different bursting kinetics. *Science* 332, 472–474.
- Suter, D.M., Molina, N., Naef, F., and Schibler, U. (2011b). Origins and consequences of transcriptional discontinuity. *Curr. Opin. Cell Biol.* 23, 657–662.
- Swinstead, E.E., Miranda, T.B., Paakinaho, V., Baek, S., Goldstein, I., Hawkins, M., Karpova, T.S., Ball, D., Mazza, D., Lavis, L.D., et al. (2016). Steroid Receptors Reprogram FoxA1 Occupancy through Dynamic Chromatin Transitions. *Cell* 165, 593–605.
- Tantale, K., Mueller, F., Kozulic-Pirher, A., Lesne, A., Victor, J.M., Robert, M.C., Capozi, S., Chouaib, R., Bäcker, V., Mateos-Langerak, J., et al. (2016). A single-molecule view of transcription reveals convoys of RNA polymerases and multi-scale bursting. *Nat. Commun.* 7, 12248.
- Thévenaz, P., Ruttimann, U.E., and Unser, M. (1998). A pyramid approach to subpixel registration based on intensity. *IEEE Trans. Image Process.* 7, 27–41.
- Veldhuis, J.D., Iranmanesh, A., Lizarralde, G., and Johnson, M.L. (1989). Amplitude modulation of a burstlike mode of cortisol secretion subserves the circadian glucocorticoid rhythm. *Am. J. Physiol.* 257, E6–E14.
- Vincent, L., and Soille, P. (1991). Watersheds in digital spaces: an efficient algorithm based on immersion simulations. *IEEE Trans. Pattern Anal. Mach. Intell.* 13, 583–598.
- Vitaterna, M.H., Selby, C.P., Todo, T., Niwa, H., Thompson, C., Fruechte, E.M., Hitomi, K., Thresher, R.J., Ishikawa, T., Miyazaki, J., et al. (1999). Differential regulation of mammalian period genes and circadian rhythmicity by cryptochromes 1 and 2. *Proc. Natl. Acad. Sci. USA* 96, 12114–12119.
- Voss, T.C., Schiltz, R.L., Sung, M.H., Johnson, T.A., John, S., and Hager, G.L. (2009). Combinatorial probabilistic chromatin interactions produce transcriptional heterogeneity. *J. Cell Sci.* 122, 345–356.
- Walker, D., Htun, H., and Hager, G.L. (1999). Using inducible vectors to study intracellular trafficking of GFP-tagged steroid/nuclear receptors in living cells. *Methods* 19, 386–393.
- Zenklusen, D., Larson, D.R., and Singer, R.H. (2008). Single-RNA counting reveals alternative modes of gene expression in yeast. *Nat. Struct. Mol. Biol.* 15, 1263–1271.

## STAR★METHODS

## KEY RESOURCES TABLE

REAGENT or RESOURCE	SOURCE	IDENTIFIER
<b>Antibodies</b>		
Anti-GR (M20)	Santa Cruz	Cat# sc-1004; RRID:AB_2155786
Anti-GR Pierce	ThermoFisher	Cat#MA1-150; RRID:AB_325419
Anti-GAPDH	Abcam	Cat# ab8245; RRID:AB_2107448
Alexa Fluor 647 donkey anti-rabbit antibody	Invitrogen	Cat# A31573; RRID:AB_2536183
<b>Chemicals, Peptides, and Recombinant Proteins</b>		
Corticosterone	Sigma-Aldrich	27840-100MG
FB	ThermoFisher	10438034
CSS FBS	ThermoFisher	12676029
DAPI	Roche	10236276001
Dexamethasone	Sigma-Aldrich	D4902
DMEM	ThermoFisher	11965092
Formaldehyde	Sigma-Aldrich	FI636-25ML
Glycine	Sigma-Aldrich	410225
Latrunculin A	Cayman Chemical Company	10010636
Millipore beads	EMD Millipore	16-663
Paraformaldehyde, 16%	Electron Microscopy Services	15710
RNaseA	Roche	10109142001
Sir-DNA	Cytoskeleton, Inc	# CY-SC007
SYBR Green Mastermix	ThermoFisher	4312704
tetracycline	Sigma-Aldrich	87128-25G
Trichostatin A	Sigma-Aldrich	T8552-1MG
<b>Critical Commercial Assays</b>		
NucleoSpin® RNA	Macherey-Nagel	740955.5
iScript	BIORAD	1708890
<b>Deposited Data</b>		
Raw and analyzed data	This study	GEO: GSE132502
Raw Images	Mendeley Database	<a href="https://doi.org/10.17632/tdj27yz3h9.1">https://doi.org/10.17632/tdj27yz3h9.1</a>
<b>Experimental Models: Cell Lines</b>		
Mouse: 33AP1C9	This study	N/A
Mouse: D4B2D10	This study	N/A
Mouse: 3617	Walker et al., 1999	N/A
Mouse: 3617 KOGR Stable HaloTag-GR	Paakinaho et al., 2017	N/A
Mouse: 3134	Georgel et al., 2003 (#5412)	N/A
<b>Oligonucleotides</b>		
smRNA FISH Probe TTTCTAGGCAATTA GGTACCT (Cy5 tagged)	Palangat and Larson, 2016	N/A
smRNA FISH Probe TTTCTAGAGTCGA CCTGC (Cy5 tagged)	Palangat and Larson, 2016	N/A
<b>Recombinant DNA</b>		
PonA-CFP-SKL-24xPP7 plasmid	Palangat and Larson, 2016	N/A
PP7 coat protein tagged with GFP (PCP-GFP)	Palangat and Larson, 2016	N/A
TetO1-SceI TetO vector	Roukos et al., 2014	N/A
pEGFP-coilin	Addgene	plasmid # 36906

(Continued on next page)

**Continued**

REAGENT or RESOURCE	SOURCE	IDENTIFIER
MMTV-24xPP7	This study	N/A
TetOI-MMTV-24xPP7-TetOI	This study	N/A
Software and Algorithms		
GDSC-SMLM ImageJ Plugin, University of Sussex		<a href="https://sites.imagej.net/GDSC-SMLM/">https://sites.imagej.net/GDSC-SMLM/</a>
Columbus software, Version 2.7 and 2.8	PerkinElmer, Waltham, MA	N/A
KNIME Image Processing (KNIP, Version 1.5.3.201611190650)	(Dietz and Berthold, 2016)	N/A
R (64-bit, Version 3.3.1)		<a href="https://cran.r-project.org/bin/windows/base.old/3.3.1/">https://cran.r-project.org/bin/windows/base.old/3.3.1/</a>
MATLAB		<a href="https://www.mathworks.com/products/matlab.html">https://www.mathworks.com/products/matlab.html</a>
Konstanz Information Mining (KNIME, 64-bit, version 3.2.1)	Berthold et al., 2008	N/A
Python 2.7		<a href="https://www.python.org/">https://www.python.org/</a>
Micromanager 1.4		N/A
LAPTracker algorithm	(Jaqaman et al., 2008)	N/A
ImageJ		<a href="https://imagej.net&gt;Welcome">https://imagej.net&gt;Welcome</a>
MultiStackReg ImageJ plugin (Version 1.46.2)		<a href="https://github.com/miura/MultiStackRegistration">https://github.com/miura/MultiStackRegistration</a>
DepmixS4 package		<a href="https://cran.r-project.org/web/packages/depmixS4/index.html">https://cran.r-project.org/web/packages/depmixS4/index.html</a>
custom software written in IDL	Harris Geospatial Solutions, Broomfield CO	N/A
UCSG Genome Browser		<a href="http://genome.ucsc.edu/">http://genome.ucsc.edu/</a>
Other		
Glass 96 well plates	Matrical	MGB096-1-2-LG-L
Glass 384 well plates	Matrical	MGB101-1-2-LG-L
JF549 HALO ligand	(Grimm et al., 2015)	N/A
JF646 HALO ligand	(Grimm et al., 2015)	N/A

**LEAD CONTACT AND MATERIALS AVAILABILITY**

Further information and requests for resources and reagents should be directed to and will be fulfilled by the Lead Contact, Gordon L. Hager ([hagerg@exchange.nih.gov](mailto:hagerg@exchange.nih.gov)).

**EXPERIMENTAL MODEL AND SUBJECT DETAILS****Plasmids and cell lines**

The MMTV-PP7 reporter was generated by modifying the previously described PonA-CFP-SKL-24xPP7 construct (Palangat and Larson, 2016). Briefly, the MMTV-CFP-SKL-PP7 (MMTV-PP7) transcription unit flanked by CTCF binding sites and I-SceI restriction sites was cloned into the pHAGE lentiviral vector backbone. This plasmid was used to produce viral particles and infect mouse GR knock-down cells expressing HALO-tagged GR under tetracycline (tet) regulation [3617 KOGR Stable HALOTag-GR (Paakinaho et al., 2017)]. As the parental cell line (3617; Walker et al., 1999) expresses GFP-GR in addition to the endogenous protein, both the GFP-tagged receptor and the endogenous GR gene were disrupted by using CRISPR-Cas9 technology (Sander and Joung, 2014). These cells were also infected with fluorescent coat protein lentiviral expression vector (Palangat and Larson, 2016), in which the cDNA coding for the PP7 viral coat protein that binds the PP7 RNA hairpins was fused to eGFP (PCP-GFP). Single cell clones were generated and one of them with 6 integrations of the MMTV-PP7 reporter construct (D4B2D10) was selected for further analysis. The I-SceI restriction sites flanking MMTV-PP7 were further used to clone the transcription unit into the TetOI-SceI-TetO vector (Roukos et al., 2014) in which we also introduced a puromycin resistance gene using the KpnI and Apal restriction sites. The resulting TetO-MMTV-PP7-TetO construct was transfected by electroporation into C127 cells (ATCC) expressing endogenous GR as well as PCP-GFP. We then used puromycin selection and subsequent single cell subcloning to obtain a cell line with very low expression of the PCP-FGP and 4 integrations of the MMTV-PP7 (33AP1C9 cells). Additional experiments were performed with the mouse 3134 cells (Georgel et al., 2003) which in contrast to the 3617 cells lack GFP-GR but are also derivative of the C127 cells.

Cells were grown in Dulbecco's modified Eagle's medium (DMEM, GIBCO BRL, Grand Island, NY) supplemented with 10% fetal bovine serum (FBS) (Hyclone, Logan, UT). Tetracycline (5mg/ml) was added to the medium of the D4B2D10 to regulate the expression of the GR-HALO and to suppress the expression of the short isoforms of the GFP-GR (remnants of the GFP-GR expression in the parental 3617 cells), which were detectable in the absence of tet by western blot (Paakinaho et al., 2017).

For the introduction of the GR-HALO into the genome of 33AP1C9 cells, 200,000 cells were plated in 6 well plates. 24 hours after plating, the cells were infected with a lentivirus which directs the expression of the Tet Repressor DNA binding domain (DBD)-VP16 activation domain fusion protein and a blasticidin resistance marker for selection. Purified lentiviral virions we mixed with 12ml of complete media (DMEM plus 10% FBS) supplemented with 5ug/ul polybrene. The media was removed from the C127 cells by aspiration and replaced with the virus containing media (2 mL per well). The 6 well plate was centrifuged at 3000 rpm for 90 minutes and returned to a 37°C humidified incubator. 48 hours after infection the cells were trypsinized and transferred to a T75 flask. Virus infected cells were selected with 10 $\mu$ g/ml blasticidin for 2 weeks. HALO-tagged rat GR was cloned into the pRevTRE retroviral vector from Takara/Clontech under control of a minimal CMV promoter preceded by 7 copies of the Tet operator. The vector also contains a hygromycin resistance gene under the control of retroviral LTR. Retroviral particles were generated in the Phoenix-AMPHO packaging cell line cell line (ATCC CRL-3213). 5 million Phoenix cells were plated in 10 cm dish in complete growth media (DMEM plus 10% FBS). 24 hours later the cells were fed with fresh media and transfected with pRevTRE-HALO-GR construct using Jet-Prime transfection reagent (Polyplus) and incubated at 32°C to increase virus stability. 48 hours after transfection the virus containing supernatant was collected and filtered through a Millex-HA 45 $\mu$ m syringe filter. The virus was diluted 1:2 with fresh growth media containing a final concentration of 5ug/ul polybrene and 10 $\mu$ g/ml tetracycline. 2ml of viral supernatant was added to 200,000 per well in a 6 well plate of C127-TetR-VP16 cells or D4 GR DNA binding domain (DBD)CRISPR knock out C127 derived cells that contain the TetR-VP16 fusion (Walker et al., 1999) that were plated 24 hours before virus collection and centrifuged at 3000 rpm for 90 minutes. The cells were returned to a 32C incubator. 48 hours post infection the cells were trypsinized and transferred to a T75 flask, and virus-infected cells were selected with 500 $\mu$ g/ml hygromycin and 10 $\mu$ g/ml tetracycline for 2 weeks. All cells were maintained in growth media supplemented with 10 $\mu$ g/ml tetracycline to prevent HALO-GR expression. Induction of HALO-GR was accomplished by changing the media to DMEM + Dextran charcoal-stripped serum (CSS) in the absence of tetracycline.

## METHOD DETAILS

### **Zeiss LSM780 life cell imaging of TSs**

Prior to live cell imaging on the Zeiss LSM780 confocal microscope, the cells were transferred into 35mm glass bottom dishes (MatTek Corporation, Ashland, MA) at a density of  $2 \times 10^5$  in Phenol Red free DMEM medium containing 10% charcoal stripped fetal bovine serum (Hyclone, Logan, UT) for at least 18h. Tetracycline was present in the media of the D4B2D10 cells to suppress the expression of GFP-GR isoforms. Cells were induced by adding 100nM Dex or 600nM Cort, unless stated otherwise. Imaging experiments were carried out on a Zeiss LSM780 confocal microscope with 60X 1.463-N.A. Oil immersion objective and the cells were kept at 37°C using an air stream stage incubator (Nevtek). Images were acquired every 60 s using the 488nm line from a 45-mW argon laser operating at 0.05% laser power and a photon counting mode.

### **Manual tracking of TSs**

TSs tracking was performed with the 'TrackRecord' software developed in MATLAB (The Matworks Inc.) (Mazza et al., 2013). Combined with a package for single-particle and single-molecule tracking molecules (Crocker and Grier, 1996). A region of interest encompassing the nucleus was selected based on a maximum projection image from the entire time laps. Potential TSs were identified in each frame of the movie based on a user-defined intensity threshold after applying Wiener, top-hat and size filters that respectively removed speckle noise, corrected for uneven illumination, and highlighted features that were around 5 pixels in area. If multiple peaks were found within a radius of 7 pixels of each other, only the brightest pixel was retained. Each seed was then fit to a two-dimensional Gaussian to precisely determine its position and the intensity of the TS. TSs in each frame were connected into trajectories using a nearest-neighbor algorithm (Crocker and Grier, 1996) with sites allowed to move a maximum of 4 pixels from 1 frame to the next. Single-frame gaps in trajectories that could result from short RNA OFF periods were filled with the average position of the site in the existing flanking frames. All tracks were curated and the gaps in the positions during the OFF times were manually filled in assuming most likely positions in respect to the nuclear topology. Only tracks from unambiguously traceable TS were kept. Resulting intensity traces were fitted to a 2state HMM model and ON and OFF times segmented.

### **GFP-GR translocation experiments**

Cells from the GFP-GR-expressing cells line, 3617 (Walker et al., 1999) were plated in 96 well plates at 15000 cells per well and grown overnight in DMEM medium containing 10% charcoal stripped serum (Hyclone, Logan, UT) without tetracycline to allow the expression of GFP-GR. Cells were then treated with vehicle control, 100nM Dex or 100nM Dex combined with 1nM Nocodazole and 1  $\mu$ M Jasplakinolide for 30 minutes. Upon treatment, cells were fixed with 4% paraformaldehyde in PBS for 10 min, washed 3 times with PBS and counterstained with DAPI. After 3 final washes with PBS cells were stored in PBS at 4°C or imaged immediately. A PerkinElmer (Waltham, MA) Opera QEHS High-Content Screening platform was used for fully automated confocal collection of

images. This system employed a  $40 \times$  water immersion objective lens, laser illuminated Nipkow disk, and cooled CCD cameras to digitally capture high-resolution confocal fluorescence micrographs (300 nm pixel size with  $2 \times 2$  camera pixel binning).

### Immunostaining

Cells (33AP1C9) were plated in 384 well plates (Matrical, Catalog Number MGB101-1-2-LG-L) at 8000 cells per well and allowed to grow for 48h DMEM medium containing 10% charcoal stripped fetal bovine serum (Hyclone, Logan, UT). Cells were induced by addition of 100nM Dex for 0, 1 and 12h. Upon treatment, cells were fixed with 4% paraformaldehyde in PBS for 10min and washed 3x with PBS. Following permeabilization with 0.5% Triton X-100 for 10min and 3 washes with PBS, cells were blocked with 3% BSA in PBS for 20 minutes. After 3 additional washes with PBS, cells were incubated with 30  $\mu$ L of anti-GR antibody (M20, Santa Cruz) diluted to 1  $\mu$ g/ml in PBS containing 3% BSA and 0.05% Triton X-100 for 1h at room temperature. Cells were further washed with PBS (3x) and incubated with Alexa Fluor 647 donkey anti-rabbit secondary antibody (Invitrogen) at 1:1000 dilution (in PBS containing 3% BSA and 0.05% Triton X-100) for 30 min at room temperature, washed with PBS (3x), and counterstained with DAPI. After 3 final washes with PBS cells were stored in PBS at  $4^{\circ}\text{C}$  or imaged immediately using the PerkinElmer (Waltham, MA) Opera QEHS High-Content Screening system.

### Automated analysis of nuclear and cytoplasmic fluorescence

A PerkinElmer (Waltham, MA) Opera QEHS High-Content Screening platform was used for fully automated confocal collection of images. This system employed a 60x water immersion objective lens, laser illuminated Nipkow disk, and cooled CCD cameras to digitally capture high-resolution confocal fluorescence micrographs (300 nm pixel size with  $2 \times 2$  camera pixel binning). An image analysis pipeline was customized using the Columbus software (PerkinElmer) to automatically segment the nucleus using the DAPI channel and then construct a ring region (cytoplasm) around the nucleus mask for each cell in the digital micrographs. As previously described (Stavreva et al., 2012a) the GR intensity of the 3617 cells (GFP-GR) or the immunoassayed 33Ap1C9 cells was calculated for both nucleus and the cytoplasm and the measurements per well were averaged and normalized to the control treatment.

### Concentration- and time-dependent induction of TSs

33AP1C9 cells were seeded in 96 well plates (Matrical, Catalog Number MGB096-1-2-LG-L) at a density of 30-40,000 cells/per well in Phenol Red free DMEM medium containing 10% charcoal stripped fetal bovine serum and induced using increasing concentrations of Dex and Cort for 1h, followed by fixation with 4% paraformaldehyde in phosphate buffered saline (PBS). DAPI counterstaining was used for improved nuclear segmentation. For the time-dependent activation response, 33AP1C9 cells were treated at 10 minutes intervals with fixed concentration of Dex and Cort (100nM and 600nM, respectively) for up to 100 minutes. Cells were fixed with 4% paraformaldehyde in phosphate buffered saline (PBS) and counterstained with DAPI. Imaging experiments were carried out on a PerkinElmer (Waltham, MA) Opera QEHS High-Content Screening system. Average number of TS/Cell was calculated using Columbus software (Version 2.7 and 2.8, PerkinElmer, Waltham, MA) and plotted as a function of hormone concentration.

### smRNA FISH experiments

33AP1C9 cells were grown in 96 well plates (Matrical, Catalog Number MGB096-1-2-LG-L) and treated with 100nM Dex or 600nM Cort for 0, 1, 4, 6, and 12h before fixation with 4% paraformaldehyde in phosphate buffered saline (PBS). PP7 probe sets (2 probes) were designed from the linker region between the repeats and ordered from Biosearch Stellaris using Quasar 670 dye (Palangat and Larson, 2016). Single molecule RNA FISH (smRNA FISH) was performed using the manufacturer's protocol with minor modifications. Fixed samples were washed with PBS and incubated in 70% ethanol for at least 1h to overnight at  $4^{\circ}\text{C}$ . Hybridized samples were counterstained with DAPI and stored in PBS at  $4^{\circ}\text{C}$  or imaged immediately. Imaging experiments were carried out on a Yokogawa CV7000 high-throughput spinning disk microscope.

### smRNA FISH imaging conditions

For smRNA FISH experiments, the image acquisition conditions were similar to the ones for short live-cell imaging, except that the samples were imaged at RT in PBS, the image Z stacks were composed of 13 images at 0.5  $\mu\text{m}$  intervals in 96 fields of view, and an additional, sequential, exposure using the 405nm laser, the 405/488/561/640nm excitation dichroic mirror, the 561nm emission dichroic mirror, and emission BP445/45 mirror was used.

### smRNA FISH data analysis

The number of smRNA FISH spots (corresponding to the MMTV-PP7 transcripts) per cell as well as the intensity of each RNA spot was calculated using Columbus software (Version 2.7 and 2.8, PerkinElmer, Waltham, MA). Experiments were performed 2 times in duplicates. As smRNA FISH measures RNA level accumulation over time, this accumulation becomes additive on a log scale and the total number of RNA per cell can be approximated to a log-normal distribution (Bengtsson et al., 2005). Using Maximum likelihood estimation (MLE) and the number of RNA per cell, the parameters of a two component Log-Normal distribution were estimated. The first component corresponds to cells that are not actively transcribing, and the parameters were extracted from the distribution of RNA per cell before induction ( $\mu = 2.07 \pm 0.24$ ;  $\sigma = 0.17 \pm 0.02$ ). The second component corresponds to cells that are actively transcribing.

The Empirical Cumulative distribution function was plotted with the theoretical fitting using the Kaplan-Meier estimate (Kaplan and Meier, 1958).

$$A_1 f(x | \mu, \sigma) + A_2 f(x | \mu_2, \sigma_2) \quad (\text{Equation 1})$$

$$f(x | \mu, \sigma) = \frac{1}{x\sigma\sqrt{2\pi}} e^{-\frac{(\ln x - \mu)^2}{2\sigma^2}} \quad (\text{Equation 2})$$

The proportions of each population were calculated with the relative weights A1 and A2.

### **Yokogawa CV7000 live cells imaging conditions**

Live-cell high-throughput imaging experiments were performed using a Yokogawa CV7000 high-throughput dual spinning disk confocal microscope. Cells were incubated in an environmental chamber at 37°C, 5% CO<sub>2</sub> and 80% humidity in 96-well plates (Matrical, Catalog Number MGB096-1-2-LG-L) in 100 µL of growth medium [Phenol Red free DMEM medium containing 10% charcoal stripped fetal bovine serum (Hyclone, Logan, UT)]. When required, cells were stained with 100nM SiR-Hoechst (SiR-DNA) dye (Cyto-skeleton, Inc.) for 30 minutes prior to imaging. Cells were induced by the addition of 100nM Dex or 600nM Cort, unless stated otherwise. Image z stacks of 15 planes at a 0.5µm interval were acquired using a heated Olympus PlanApoChromat 60X water lens objective (NA 1.2), and 2 sCMOS cameras (2550 X 2160 pixels) using camera binning of 2X2. Samples were simultaneously excited with 488nm and 640nm lasers using a 405/488/561/640 nm excitation dichroic mirror, and fluorescent signals were collected using a 561nm emission dichroic mirror and BP525/50 and BP676/29 mirrors in front of the 2 sCMOS cameras, respectively. Depending on the experiment, image Z stacks were acquired every 10, 60, or 100 s intervals at every field of view. A total of 1, 12, and 16 fields of view were acquired at 10, 60, or 100 s, respectively. Images were corrected on the fly using a geometric correction for camera alignment and optical aberrations, then a flat field correction for illumination patterns, and finally projected in 2D using maximal projection. Images were saved and stored as 16-bit TIFF files.

### **Long-term Induction experiments**

For long-term imaging experiments (4 days), the conditions were like the ones above, except that a 40X Olympus PlanApoChromat air objective (NA 0.9) was used to acquire Z stacks of 9 images only in the 488 nm channel every 1.0 µm and at 30min intervals in 16 fields of view.

### **Hormone withdrawal experiments**

Cells were seeded into 96 well plates were induced with 600nM Cort, and 30min time lapses were taken for 12h under continuous incubation (37°C, 5%CO<sub>2</sub>) using a heated Olympus PlanApoChromat 60X water lens objective (NA 1.2) and 488nm laser at 5% power and 250ms exposure time. Media were then replaced with hormone-free media and the cells were returned to the incubated stage and imaged for an additional 12h at 30min intervals. A final round of imaging under identical conditions was performed after subsequent stimulation with 600nM Cort. Numbers of TSs/Cell was calculated using Columbus software (Version 2.7 and 2.8, PerkinElmer, Waltham, MA) and plotted as a function of time.

### **Ultradian life cell experiments**

Cells (33AP1C9) stained with 100nM SiR-DNA dye for 30 minutes were treated with 600nM Cort and imaged for 20 minutes at 100 s intervals. The imaging was then stopped, cells were washed 3x with pre-warmed (37°C) hormone-free medium supplemented with the SiR-DNA dye, and the imaging was resumed for additional 40 minutes. A second round of the protocol was performed to collect data for the subsequent hormonal pulse. The resulting 4 individual time lapse movies were then combined to generate a composite time lapse which was analyzed using a modified KNIME workflow (see below).

### **Yokogawa CV7000 high-throughput data processing**

#### **Image analysis workflows**

Briefly, the image analysis workflow was comprised of the following main modules (see Figure S2A): (i) segmentation (Soille, 2013; Vincent and Soille, 1991) and tracking (Jaqaman et al., 2008) of fluorescently labeled cells (e.g., PP7 bacteriophage coat protein fused to green fluorescent probe) in the field of view of 2D time-lapse images, acquired on an automated, high-throughput spinning disk confocal microscope (Yokogawa, Cell Voyager 7000S); (ii) automatic sub-pixel registration (affine/rigid body) of cells in time-lapse movies (Thévenaz et al., 1998); (iii) automatic detection (GDSC-SMLM ImageJ Plugin, University of Sussex, <https://sites.imagej.net/GDSC-SMLM/>) and tracking of (Jaqaman et al., 2008) multiple fluorescently-tagged transcription sites in individual living cells; (iv) extracting temporal intensity trajectories of each transcription sites; and (v) kinetic modeling [6] of the transcription bursts in the temporal intensity trajectories.

All image processing workflows were implemented using open-source workflow orchestration and management software, Konstanz Information Mining (KNIME, 64-bit, version 3.2.1) (Berthold et al., 2008) with KNIME Image Processing (KNIP, Version 1.5.3.201611190650; Dietz and Berthold, 2016), R (64-bit, Version 3.3.1) and Python (64-bit, Version 2.7.12) scripting nodes. All 2D time-lapse images from the CV7000S microscope were analyzed using bespoke KNIME workflows on a HP Blade Workstation with 64-bit Windows 2012 R2 operating system, 256GB RAM and 16 core AMD Opteron(TM) 6212 processors (2.6 GHz).

### Segmentation and tracking of live cells

The nuclei in the field of view (FOV) from the maximum intensity projection (MIP) of the SiR-Hoechst (SiR-DNA) channel were segmented using a seeded watershed algorithm (Vincent and Soille, 1991). The seeded watershed algorithm, typically, requires seeds points/regions and edge information. To automatically generate the starting seeds, we first applied OTSU thresholding (Otsu, 1979) to the SiR-Hoechst channel and then the ultimate eroded points in the Euclidean distance map of the OTSU thresholded bitmask. For extracting the edge information, we summed the directional morphological gradients in four orientations (0, 45, 90, and 135 degrees) using a line structuring element with radius of three pixels (Legland et al., 2016). This segmentation approach was routinely used for segmenting fluorescently stained cells/nuclei (Pinidiyaarachchi and Wählby, 2005), but it had two major shortcomings. First, the approach could not resolve boundaries between overlapping nuclei. Second, it was prone to over-segmentation, that is, splitting one single nucleus into multiple objects. Hence, we used a supervised two-class, namely, *GoodSegmentedNucleus* and *BadSegmentedNucleus*, Random Forest (RF) classifier (Breiman, 2001) to filter out bitmasks corresponding to overlapping nuclei as well as any over-segmented nuclei (Gudla et al., 2017; Jowhar et al., 2018a; Jowhar et al., 2018b). In order to generate the training data for the supervised RF classifier, a user-interactive version of KNIME workflow was used for annotating segmented objects from FOVs. The FOVs were selected at linearly sampled time points in the 2D time-lapse image series. The end user identified and annotated at least 50 objects per class (*GoodSegmentedNucleus* and *BadSegmentedNucleus*). Next, we calculated morphometric features (e.g., circularity, area, perimeter, and major/minor elongation) for each of the annotated object using the 2D geometric feature set from the KNIP Feature Calculator node. These extracted features along with the annotated class label were used to train a supervised, two-class RF classifier using KNIME Tree Ensemble Learner node. We, typically, generate one RF classifier per cell-line using a few time points from an FOV corresponding to a cell-line and applied it to all 2D-t image series for that cell-line. The filtered segmentation bitmasks of nuclei in the FOVs of 2D-t image series were then used for tracking individual nuclei using the LAPTracker algorithm without any gap closing (Jaqaman et al., 2008). After tracking the nuclei, we only retained 2D-t nuclei that are visible in the first frame ( $T_{start}$  = 1st frame) of the 2D-t image series and continued to appear (were tracked) in the FOV for at least half of the time lapse experiment (e.g.,  $T_{end}$  = 312nd frame). The tracked 2D-t bitmasks of nuclei were then used for cropping SiR-Hoechst and MMTV-PP7-GFP channels.

### Registration of tracked 2D-t cells

To facilitate accurate tracking of multiple transcription sites in a single nucleus, we applied automatic sub-pixel registration algorithm to spatially register/align (Thévenaz et al., 1998) the SiR-Hoechst intensity channel of a nucleus along the temporal dimension. Briefly, the registration algorithm operated by first estimating the rigid-body (affine) transformation between two successive frames of the 2D-t stack by minimizing the mean square difference of intensities between the target (reference) and source (moving) frames. Next, the algorithm used this local transformation to spatially align/register the nucleus (based on SiR-Hoechst intensity) along the entire time series. The target (reference) frame in our registration implementation was always set to the first time point ( $T = 0$ ) in the 2D-t stack. We used the KNIP ImageJ Macro node to invoke the MultiStackReg ImageJ plugin (Version 1.46.2, <https://github.com/miura/MultiStackRegistration>) for estimating the global rigid-body/affine transformation. Subsequently, we spatially aligned/registered the MMTV-PP7-GFP channel of the tracked nucleus using the inverse of the global (rigid/affine) transformation matrix estimated for the SiR-Hoechst channel. As separate instance of KNIP ImageJ Macro node in our KNIME workflows invoked the necessary MultiStackReg plugin for applying the transformation to MMTV-PP7-GFP channel of the tracked nucleus.

### Detection and tracking of multiple TSs

The MMTV promoter sites in the MMTV-PP7-GFP channel of the tracked nucleus were detected using the Peak Fit routine from GDSC-SMLM ImageJ/Fiji Plugin. The peak finding algorithm finds maximas (peaks) in the 2D-t image series and fits them using a 2D Gaussian. A customized configuration capturing our image acquisition setup and sample conditions was used in the Peak Fit routine.

The Peak Fit routine, however, would also find false positive peaks corresponding to shot noise in the MMTV-PP7-GFP channel. We used a separate supervised, two-class (*GoodSpot* and *BadSpot*) Random Forest Classifier (Breiman, 2001) based on the 2D Gaussian fit parameters to filter out these false positive peaks. A separate standalone, interactive KNIME workflow allowing the end-user to select the MMTV-PP7-GFP channel of tracked nuclei generated by the FOV segmentation and tracking KNIME workflow and Peak Fit routine was used to detect potential (*GoodSpot* and *BadSpot*) maximas corresponding to the GFP-tagged MMTV transcription sites. The end user then manually selected and annotated at least 50 instances of both *GoodSpot* and *BadSpot* objects corresponding to the true GFP-tagged MMTV promoter sites and background (shot) noise, respectively. Note, the annotated objects can originate from multiple tracked 2D-t nuclei. The annotated objects along with their 2D Gaussian parameters (e.g., signal, uncertainty, sigma, background/offset) were used for training the RF Classifier. As with nucleus segmentation, we generated one RF Classifier per cell-line/clone for filtering out false positive peaks from MMTV-PP7-GFP channel in tracked nuclei. We subsequently applied the trained RF Classifier for filtering out false positive peaks in the MMTV-PP7-GFP channel on all our tracked nuclei for a cell-line/clone originating from multiple fields in a well and/or multiple wells.

Next, we constructed a binary image using the X and Y centers of true positive peaks from the Peak Fit routine. The spatial and temporal dimensions of this binary image were identical to the fluorescent image(s) of the tracked nuclei. We transformed (rigid/affine) the 2D-t binary image comprising of the 2D Gaussian centers to the registered SiR-Hoechst channel. The bitmasks of the 2D Gaussian centers in this registered space were then tracked throughout the time-lapse using the LAPTracker algorithm with gap closing (Jaqaman et al., 2008). Tracking of the peaks, corresponding to GFP-tagged MMTV promoter sites, in the registered space

permitted reliable and robust tracking of multiple TSs in a single nucleus/cell. The LAPTracker algorithm also assigned a unique track number to the collection of peaks (GFP-tagged transcription sites).

#### **Extraction of Temporal Intensity Trajectories**

After the true-positive peaks were tracked by the LAPTracker algorithm, we reverted the transformation to bring back the X and Y coordinates of each peak (GFP-tagged MMTV site) in a track to the original (unregistered) coordinate system of the GFP channel. We subsequently extracted background corrected, 2D Gaussian weighted intensity around the center of each true positive peak (GFP-tagged MMTV promoter site). For frames in which the prompter was absent (was not detected by Peak Fit routine or was detected but filtered out by our supervised RF Classifier), we linearly interpolated the last known X and Y coordinate of the TS for intensity calculation.

#### **Hidden Markov Modeling**

We applied a 2-state (ON/OFF), zero-order Hidden Markov model (HMM) for discretizing (converting) the intensity trajectory of each transcription site and the two states were assumed to be Gaussian distributed. The HMM was applied to each trajectory independently. After fitting the intensity trajectory to a 2-state model, we also extracted epochs of ON and OFF times in the trajectory. Trajectories from multiple nuclei (typically over 100) of the same clone were used for generating a cumulative distribution of the ON and OFF periods.

The HMM analysis was carried out using the functions from DepmixS4 package (<https://cran.r-project.org/web/packages/depmixS4/index.html>) for R (64-bit, Version 3.3.2). The customized R script was embedded into our KNIME workflow using the R-Scripting KNIME node from KNIME Labs.

#### **Single molecule tracking (SMT) Experiments**

The D4B2D10 cells (or 33AP1C9 cells, expressing HALO-tagged GR) were plated into two-well Lab-Tek chamber slides (Thermo Fisher, Waltham, MA, USA) in Phenol Red free DMEM medium containing 10% charcoal stripped fetal bovine serum (Hyclone, Logan, UT) for at least 18 h. The next day cells were incubated with 0.25nM of cell permeable Janelia Fluor 549 HALOTag ligand (JF549; Grimm et al., 2016) for 20min. Cells were then washed extensively (3 rounds of 3 washes separated by 15 minutes) with phenol red-free DMEM media (Invitrogen) to remove the unbound fluorescent molecules and treated with 600nM of Cort or 100nM Dex for the indicated times. For the 12h-treatment experiments, cells were plated in Phenol Red free DMEM medium for ~18h as described above, treated with 600nM of Cort or 100nM Dex for 10h and stained with JF549 dye for 20min. The subsequent washes were carried in the presence of the ligands and the cells were then imaged for ~2h.

A custom-built microscope (Optical Microscopy Core facility, LRBGE, NCI) controlled by Micro-Manager software (Open Imaging, Inc., San Francisco, CA.) was used. It was equipped with a 150, 1.45 numerical aperture objective (Olympus Scientific Solutions, Waltham, MA), a 561nm laser (iFLEX-Mustang, Excelitas Technologies Corp., Waltham, MA), an acousto-optic tunable filter (AOTFnC- 400.650, AA Optoelectronic, Orsay, France) and HILO (highly inclined and laminated optical sheet) illumination microscope. Eight-hundred frames of fluorescent images were collected on an EM-CCD camera (Evolve 512, Photometrics) at a rate of 5Hz with 10ms exposure time to determine the bound and unbound GR fraction, while a rate of 2Hz with 500ms exposure time was used for the remaining SMT experiments.

The particle tracking was performed with the ‘TrackRecord’ software developed in MATLAB (The Matworks Inc.) (Mazza et al., 2013). The software combined a package for single-particle and single-molecule tracking with the routines to isolate chromatin-bound molecules (Crocker and Grier, 1996; Presman et al., 2017). A region of interest encompassing the nuclear compartment was selected based on a maximum projection image from the 800 frames stack. Potential particles were located in each frame of the movie based on a user-defined intensity threshold after applying Wiener, top-hat and size filters that respectively removed speckle noise, corrected for uneven illumination, and highlight features that are around 5 pixels in area. Each molecule was then fit to a two-dimensional Gaussian to precisely determine its position. Particles in each frame were connected into trajectories using a nearest-neighbor algorithm (Crocker and Grier, 1996) with molecules allowed to move a maximum of 2 pixels from 1 frame to the next for the (2Hz acquisition) and 4 pixels for 5Hz acquisition, and only tracks that were at least 2 frames long were kept.

The bound population of the tracks was then extracted by comparison with core histone H2B displacement measurement. H2B maximum 99% frame-to-frame displacement ( $R_{\text{min}}$ ) and maximum two-frame 99% displacement ( $R_{\text{max}}$ ) were established (210 nm and 270 nm for the 2Hz acquisition and 270 nm and 310 nm for the 5Hz acquisition, respectively). To be considered further in the analysis, GR tracks displacements should be equal to or lower than the H2B displacement values. Single GR molecules that were moving for a distance larger than  $R_{\text{min}}$  or  $R_{\text{max}}$  were considered unbound. The residence time of GR was estimated from the remaining bound population.

Tracks distribution was then compiled and analyzed using a novel pipeline for data analysis (Garcia et al., 2019). Photobleaching kinetics were determined by fitting a triple exponential component to H2B residence time ( $32 \pm 1.05$  s). The survival distribution of GR was corrected using the distribution from the photobleaching estimate and was fitted to four different models (for details see Garcia et al., 2019). Using BIC, the best predicting model for the distribution of the GR residence times was a power law.

#### **Western blot analyses**

33AP1C9 cells were grown in DMEM medium containing 10% charcoal stripped fetal bovine serum (Hyclone, Logan, UT) for at least 18 h and treated with 600 nM Cort for 0, 1 and 12h. Upon treatment cells were washed in phosphate buffered saline, lysed in whole

cell lysis buffer [20 mM HEPES, pH 7.6, 20% Glycerol, 1.5 mM MgCl<sub>2</sub>, 0.2 mM EDTA, 0.1% Triton X-100, 1 mM DTT, and 1x complete protease inhibitors cocktails (Roche, Indianapolis IN)] containing 500mM NaCl for 30 min., and pelleted by microcentrifugation at top speed. Protein levels were quantified (BioRad) and 20 $\mu$ g of protein was boiled at 95°C for 5 minutes and proteins were then separated by SDS-PAGE and transferred to PVDF membranes. Blots were probed with the anti-GR (M20, sc-1004) or anti-GAPDH (Abcam, ab8245) antibodies in Tris buffered saline (TBS) containing 5% nonfat dry milk, followed by incubation with horseradish peroxidase (HRP) conjugated anti-goat antibody (Santa Cruz Biotechnology, Santa Cruz CA). All blots were visualized with the ECL kit (Super-signal West Dura, Pierce, Rockford IL).

#### GR chromatin immunoprecipitation (ChIP) and ChIP-seq

33AP1C9 cells were grown in steroid-depleted medium for 24h prior to collection and were either treated with 600nM of Cort (Sigma) for 1h or 12h or left untreated. The cells were cross-linked with 1% (v/v) paraformaldehyde (Electron Microscopy Sciences) for 5min and subsequently quenched with 150mM glycine for 5min. The cells were rinsed twice with ice-cold PBS and collected in ice-cold PBS containing Protease Inhibitor Cocktail (Sigma). After collection, the cell pellets were resuspended in ChIP Lysis Buffer [0.5% (w/v) sodium dodecyl sulfate (SDS), 10mM EDTA, 50mM Tris-HCl (pH 8), protease inhibitor cocktail]. Chromatin was sonicated (Bioruptor, Diagenode) to an average DNA length of 200–500bp and cellular debris was removed by centrifugation. After determining the chromatin concentration, the samples were diluted with ChIP Dilution Buffer [0.01% (w/v) SDS, 1.2mM EDTA, 16.7mM Tris-HCl (pH 8), 1.1% (v/v) Triton X-100, 167mM NaCl, protease inhibitor cocktail] to concentration of 200  $\mu$ g per ml of chromatin. For immunoprecipitation, 600ug of chromatin was incubated with magnetic bead-conjugated (Millipore) GR antibody cocktail (Thermo MA1-510, Santa Cruz #SC-1004) with rotation overnight at 4°C. The beads were harvested by magnets and washed once for 5min at 4°C by gentle shaking with 1ml of ChIP Low Salt Wash Buffer [0.01% (w/v) SDS, 2 mM EDTA, 20mM Tris-HCl (pH 8), 1% (v/v) Triton X-100, 150mM NaCl], 1ml of ChIP High Salt Wash Buffer [0.01% (w/v) SDS, 2mM EDTA, 20mM Tris-HCl (pH 8), 1% (v/v) Triton X-100, 500 mM NaCl], and 1ml of ChIP LiCl Wash Buffer [250mM LiCl, 1% (w/v) IGEPAL, 1% (w/v) sodium deoxycholate, 10mM Tris-HCl (pH 8), 1 mM EDTA]. Finally, the beads were washed two times for 2min at 4°C with 1 mL of TE buffer [1 mM EDTA, 10 mM Tris-HCl (pH8)]. Antibody-bound chromatin fragments were digested with proteinase K (Thermo) for 2 h at 50°C and cross-linking was reversed for 7h at 65°C. DNA was purified with phenol-chloroform extraction followed by ethanol precipitation and washed twice with 70% ethanol. Primers used for amplification of the promoter region of *MMTV* (NucB), the promoter of *Tgm2* gene and the enhancer involved in the regulation of the *Tsc22d3* gene (Stavreva et al., 2015) were: NucB: sense 5'-TTAAGTAAGTTTTGGTT CAAACT-3' and antisense 5'-TCAGAGCTCAGATCAGAACCTTGATACC-3'; *Tgm2*: sense 5'-CCACACATTGGTTTGCTATG CTTG-3'; and antisense 5'-AATCATTTCTCATTCCACACAGCC-3'; *Tsc22d3* enhancer: sense 5'-GGGACAGTGATTCCCCAAC-3' and antisense 5'-TTTCTCTGGCCTGTTGGTC-3'.

ChIP-seq libraries were generated by using the Illumina TruSeq Chip Sample Prep Kit (Illumina # IP-202-1012) according to manufacturer's instructions. ChIP-seq data were aligned to mm10 and further analysis was performed using HOMER as described in Heinz et al. (2010). Peaks in each dataset were called using "findPeaks" with the style factor for TFs. An input sample from the vehicle condition was used as the control for the IP samples and resulted in only one called peak for the vehicle condition. Peak filtering was done with the following parameters; FDR < 0.001, > 6 FC over control, > 6 FC over local background, and > 75 tags per site. The "mergePeaks" command with "-prefix" option was used to distinguish shared/unique peaks between the 1 h and 12 h treatment samples. The "annotatePeaks.pl" with "-hist 20 -size 2000 -ghist" options were used to generate heatmap matrices.

#### Gene expression studies by RT-qPCR

Gene expression studies were performed in a specially adapted incubator, allowing media replacement under conditions of stable CO<sub>2</sub> and temperature levels throughout the duration of an experiment. 33AP1C9 cells were treated with 2 pulses (20min each) of 600 nm Cort, interspersed with 40-minute periods of incubation with hormone free media and samples were collected every 5 minutes. For the experiments comparing the 1h versus 12h of Cort stimulation, cells were treated constantly with the hormone and samples were collected at the indicated times.

Circadian experiments were performed using 3134 cells (Fragoso et al., 1998), which similarly to D4B2D10 and 33AP1C9 cells, are derived from the C127 cells. The 3134 cells were plated in 6 well plates in Phenol Red free DMEM medium containing 10% charcoal stripped fetal bovine serum (Hyclone, Logan, UT) overnight and then subjected to 36h of constant or ultradian Cort (600nM) treatment. Both treatments were performed in the adapted incubator (see above) and the ultradian treatment consisted of 8 hormonal pulses [(20-minutes each), interspersed by 40 minutes of hormone-free media] followed by a 16h of uninterrupted hormone withdrawal period. This treatment was repeated twice (see also Figure S1O) and samples were collected every 6h in duplicate. 3134 cells were also used to detect gene-specific time-dependent changes in the expression of GR-regulated genes. Treatment with 600nM Cort was carried out for up to 8h and samples were taken at 1h intervals.

Total RNA was extracted, reverse transcribed (iScript cDNA) and used in qPCR reaction applying SyBr green and Bio-Rad IQ system (Biorad, Hercules, CA). Primers used to detect the mature *Per1* RNA were: 5'-TGAAGCAAGACCGGGAGAG-3' (sense) and 5'-CACACACGCCGTACATCAA-3' (antisense); the sequences designed to amplify nascent RNA (amplicons that cross an exon-intron boundary) of the *p21* gene were: 5'-GTACTCCTCTGCCCTGCTG-3' (sense) and 5'-CTCTCCTCTCCAGGCCTCT-3' (antisense); the sequences of the primers for nascent *Tgm2* RNA were: 5'-TGTCAACCAGGGATGAGAGACGG-3' (sense) and

5'-TCCAAATCACACCTCTCCAGGAG-3' (antisense); and the primers for the detection of the nascent *Tsc22d3* RNA were: 5'-ACATGATGGTGGCATGAAGA-3' (sense) and 5'-TCTTCTCAAGCAGCTCACGA-3' (antisense).

### Orbital tracking

Cells were prepared similarly to the SMT experiments with minor modifications. They were grown in 35mm dishes with #1.5 cover-slips (Cellvis, Mountain View, CA) overnight in DMEM with 10% Charcoal Stripped FBS, labeled for 20 minutes with JF646 dye (Grimm et al., 2016) and induced with Dex 10-20 minutes before imaging. The sample was then placed inside a prewarmed Okolab stage incubator maintained at a temperature of 37°C, 5% CO<sub>2</sub> and 100% Humidity. Cells were imaged on the microscope for 20min to 4h after induction until transcription sites appeared as diffraction limited spots inside the nucleus of a cell. When an active transcription site was identified, the laser power was lowered to reduce photobleaching and orbital tracking was initiated according to Annibale and Gratton, 2015; Kis-Petikova and Gratton, 2004; and Levi et al., 2003, 2005a, 2005b.

Tracking of transcription sites was achieved using two orbits of radius ~87nm at a position 145nm above the transcription site. Two orbits were then performed at a position 145nm below the transcription site. Orbits consisted of 64 points per orbit with a pixel dwell time of 1024μs per pixel. This gave each orbit a duration of 65.5ms with a total sampling time of 262ms or a 3.8 Hz sampling rate. Orbital tracking allowed the measurement of GR and MMTV RNA occupancy at a high sampling rate over timescales from minutes to hours while keeping the transcription site in focus via the z-piezo and active feedback from microscope software (described below).

Fluorescence intensity appeared in carpet plots of angle versus time showing a Gaussian peak in the RNA channel with intermittent signal in the red channel representing the binding of fluorescently labeled GR molecules. Sections of the fluorescence intensity traces were selected for active transcription by the appearance of signal above background in the carpet plots. Temporal correlation functions of the fluorescent signal were calculated in the standard way from half the average photon intensity over the 4-orbital period of 262ms directly from the DC component of the fluorescence intensity trace as shown in Equation 18 of Kis-Petikova and Gratton (2004). Correlation functions were averaged over 10-20 measurements. This resulted in very robust and reproducible correlation functions from which the dwell time of GR molecules, MMTV RNA and temporal relationships could be estimated as described above.

Correlation functions were fit to models using the LMFIT package (Newville et al., 2014) in python 2.7. For autocorrelation functions, a single component exponential or sinc function was used, and for cross correlation functions, a shifted Gaussian was used. Model fits were evaluated using Bayesian Inference Criteria (BIC). The MMTV RNA autocorrelation was best fit with a sinc function; GR autocorrelation function was best fit using a single exponential fit.

For orbital tracking 488nm and 633nm excitation lasers were reduced to a point where < 25% of the signal would be lost due to photobleaching over the course of a measurement. Laser power was then kept at this constant level for future experiments. Measurements generally would last ~20 minutes to 1h.

Imaging and Orbital tracking were performed on an ISS Alba FCS microscope (Champaign, IL). 488nm and 633nm excitation was used in combination with a dual band pass filter, zet488-640 m (Chroma, Bellows Falls VT). Emitted light was split using a long pass filter, et655lp (Chroma) and emission filters, ET700/75 m (Chroma) and 525/50 (Semrock, Rochester NY). Single photon counting was performed with two SPCM-ARQH Avalanche Photodiodes (Pacer, Palm Beach, FL) with dark counts < 100/s. Data acquisition was performed using SimFCS 3.0 software written by Enrico Gratton (Laboratory for Fluorescence Dynamics, University of California, Irvine). 3D Orbital Tracking was possible using a 1MHz IOtech 3000 Data Acquisition card (Measurement Computing Corporation, Norton, MA) and a Nano-F25HS high speed z piezo (Mad City Labs Incorporated, Madison, WI) coupled to a Nikon Ti-U inverted microscope with a CFI Plan Apochromat 60X 1.2 NA water immersion objective (Nikon Instruments Incorporated, Melville, NY). Alignment of the microscope was confirmed in xyz by the 3D imaging of fluorescent beads. The point spread function alignment in both channels was estimated to be ~60nm. A 0.5-2x variable beam expander was placed in front of the 488nm laser to achieve alignment in z due to chromatic aberration. When using one photon excitation for cross correlation spectroscopy, alignment of both lasers in 3D is critical to achieve success (Schwille et al., 1999).

Data analysis was performed using custom software written in IDL (Harris Geospatial Solutions, Broomfield CO) and Python 2.7 (Continuum Analytics, Austin, TX).

### Characterization of burst ON times by autocorrelation analysis

To properly characterize the transcriptional bursting (ON time) from the intensity traces collected at 10 s and 60 s intervals, the ensemble average of the traces autocorrelation was calculated as defined in Equation 3.

$$R(\tau) = \frac{1}{N} \sum_x \frac{E[(X_t - \mu)(X_{t+\tau} - \mu)]}{\sigma^2} \quad (\text{Equation 3})$$

$$(f_1 e^{-t/\tau_{Simple}} + (1 - f_1) e^{-t/\tau_{Complex}}) \quad (\text{Equation 4})$$

The auto-correlation was best fitted by a double exponential (Equation 4) using Non-linear least-squares method. Each component was interpreted as the average ON time of simple burst and complex burst (Cai et al., 2008). The fraction of each population was calculated as the weight of each exponential component.

### Co-bursting analysis

Crosscorrelation can be used as a measure of similarity between time series (Box et al., 1994) as a function of time lag between them. The Crosscorrelation function was estimated from the sample cross covariance function between burst of different integrations for each cell. For time series  $I_{1t}$  and  $I_{2t}$ , with lags  $\eta = 0, \pm 1, \pm 2, \dots$  an estimation of the cross variance is given by:

$$r_{I_1 I_2}(\eta) = \begin{cases} \frac{1}{T} \sum_{t=1}^{T-\eta} (I_{1,t} - \langle I_1 \rangle)(\langle I_{2,t+\eta} \rangle - \langle I_2 \rangle) & \eta = 0, 1, 2, \dots \\ \frac{1}{T} \sum_{t=1}^{T-\eta} (I_{2,t} - \langle I_2 \rangle)(\langle I_{1,t-\eta} \rangle - \langle I_1 \rangle) & \eta = -1, -2, \dots \end{cases} \quad (\text{Equation 5})$$

Defining the standard deviation of the time series as  $S_{T_1}$  and  $S_{T_2}$  respectively. The cross-correlation estimate corresponds to:

$$R_{I_1 I_2}(\eta) = \frac{r_{I_1 I_2}(\eta)}{S_{T_1} S_{T_2}}; \quad \eta = \pm 1, \pm 2, \dots \quad (\text{Equation 6})$$

Crosscorrelation is not symmetric. In general,  $R_{ij}(\eta) \neq R_{ji}(\eta)$ . We create the symmetric relation  $\hat{R}_{ij}(\eta) = \frac{R_{ij}(\eta) + R_{ji}(\eta)}{2}$ . The mean and standard deviation of each time series was set to 0 and 1, respectively.

The data can be binned by dividing the distance between loci in equal spacing subunits (Figure S7 E and F and I and J). The Cross-correlation was averaged as shown in Equation 7.

$$\hat{R}(\eta)_D = \frac{1}{|D|} \sum_{ij=1}^N \hat{R}_{ij}(\eta) \chi_D(d_{ij}) \quad (\text{Equation 7})$$

Where  $\chi_D(d_{ij})$  corresponds to the step function with D:  $x \{ |D - \delta D| \leq x \leq D \}$  and  $\delta D$  corresponds to the binning spacing (0.01). The distance between burst pairs ( $d_{ij}$ ) is calculated as the root mean square distance. Let  $I_{1t}$  and  $I_{2t}$  be two mRNA burst in the same cell with position  $(x_1(t), y_1(t))$  and  $(x_2(t), y_2(t))$  respectively. The distance between them is defined in Equation 8. This distance is normalized to cell diameter to account for cell variability (Figure S7B).

$$d_{ij} = \sqrt{\frac{(x_j(t) - x_i(t))^2 + (y_j(t) - y_i(t))^2}{N}} \quad (\text{Equation 8})$$

Where N corresponds to the acquisition time (in frames) which is kept the same for all the burst. This distance is normalized with respect to the cell diameter.

$R(0)_D$  was fitted to a single exponential function to characterize the length scale for co-bursting decay for neighboring (proximal) TSs with distance. The parameter of the exponential fit, characterizes the mean length scale for the co-bursting to happen. To characterize co-bursting at longer distances, the proximal pairs (closer than 10% of cell diameter) were removed and a simple regression model was fitted to the  $R(0)_D$  (Rodriguez et al., 2019) A deviation of the slope from 0 would indicate either positive or negative cross-correlation with distance.

To characterize possible crosscorrelation delays between burst, the crosscorrelation function was projected over the time lag versus normalized distance axes, creating a contour plot in which the constant levels of crosscorrelation are displayed in different colors.

In order to test the significance of the correlations between co-bursting sites, we constructed an empirical distribution by calculating the correlation between pairs of sites in the same field of view but from different cells ( $n = 200$  pairs) without binning (Equation 9).

$$\bar{R}(\eta)_D = \hat{R}_{ij}(\eta) \delta(D - d_{ij}) \quad (\text{Equation 9})$$

This empirical null distribution has a mean correlation of 0 with a standard deviation of 0.13 (see Figures S7C and S7D). We considered any pair of sites which exhibited a correlation value greater than the 99th percentile value of the empirical null (0.338) to be significantly correlated.

In order to test whether cytoskeletal inhibition led to a preferential loss of distal co-bursting, we used bootstrap analysis. We constructed a bootstrap ensemble by randomly resampling the combined dataset of distal burst site correlations (with replacement). We then computed the ensemble difference in the proportion of sites that were classified as significant in the resampled control and drug distributions. A similar bootstrap analysis of the proportion of correlated proximal sites (defined as sites closer than  $0.2 \times$  normalized distance) was also performed.

## QUANTIFICATION AND STATISTICAL ANALYSIS

All statistical tests used are stated in the figure legends. Specific software and analysis approaches are described in detail in the relevant [STAR Methods](#) sections.

## DATA AND CODE AVAILABILITY

ChIP-seq data were deposited into GEO under the accession number GSE132502. Raw images associated with micrographs presented in the figures, a Western Blot image, and TIFF files from representative time-lapse experiments have been deposited in the Mendeley Database: <https://doi.org/10.17632/tdj27yz3h9.1>.